atmosphere

MDPI

Article

Atmosphere Driven Mass-Balance Sensitivity of Halji Glacier, Himalayas

Anselm Arndt [1,*], Dieter Scherer [2] and Christoph Schneider [1]

[1] Geography Department, Humboldt-Universität zu Berlin, 10099 Berlin, Germany; christoph.schneider@geo.hu-berlin.de
[2] Chair of Climatology, Technische Universität Berlin, 12165 Berlin, Germany; dieter.scherer@tu-berlin.de
* Correspondence: anselm.arndt@geo.hu-berlin.de

Abstract: The COupled Snowpack and Ice surface energy and mass balance model in PYthon (COSIPY) was employed to investigate the relationship between the variability and sensitivity of the mass balance record of the Halji glacier, in the Himalayas, north-western Nepal, over a 40 year period since October 1981 to atmospheric drivers. COSIPY was forced with the atmospheric reanalysis dataset ERA5-Land that has been statistically downscaled to the location of an automatic weather station at the Halji glacier. Glacier mass balance simulations with air temperature and precipitation perturbations were executed and teleconnections investigated. For the mass-balance years 1982 to 2019, a mean annual glacier-wide climatic mass balance of −0.48 meters water equivalent per year (m w.e. a^{-1}) with large interannual variability (standard deviation 0.71 m w.e. a^{-1}) was simulated. This variability is dominated by temperature and precipitation patterns. The Halji glacier is mostly sensitive to summer temperature and monsoon-related precipitation perturbations, which is reflected in a strong correlation with albedo. According to the simulations, the climate sensitivity with respect to either positive or negative air temperature and precipitation changes is nonlinear: A mean temperature increase (decrease) of 1 K would result in a change of the glacier-wide climatic mass balance of −1.43 m w.e. a^{-1} (0.99 m w.e. a^{-1}) while a precipitation increase (decrease) of 10 % would cause a change of 0.45 m w.e. a^{-1} (−0.59 m w.e. a^{-1}). Out of 22 circulation and monsoon indexes, only the Webster and Yang Monsoon index and Polar/Eurasia index provide significant correlations with the glacier-wide climatic mass balance. Based on the strong dependency of the climatic mass balance from summer season conditions, we conclude that the snow–albedo feedback in summer is crucial for the Halji glacier. This finding is also reflected in the correlation of albedo with the Webster and Yang Monsoon index.

Keywords: High Mountain Asia; Himalayas; Halji glacier; COSIPY; cryosphere; climatic mass balance variability; atmospheric forcing; seasonal sensitivity characteristics; energy and mass balance modeling; atmospheric downscaling

Citation: Arndt, A.; Scherer, D.; Schneider, C. Atmosphere Driven Mass-Balance Sensitivity of Halji Glacier, Himalayas. *Atmosphere* **2021**, *12*, 426. https://doi.org/10.3390/atmos12040426

Academic Editors: Renato R. Colucci and Edward Hanna

Received: 20 January 2021
Accepted: 22 March 2021
Published: 26 March 2021

1. Introduction

Since the 1850s, an overall glacier mass loss in High Mountain Asia (HMA), which accelerated in recent decades, has been observed (e.g., [1–6]). Shean et al. [7] estimate a total annual mass balance (MB) of (-19.0 ± 2.5) Gt a^{-1} or -0.19 ± 0.03 meters water equivalent per year (m w.e. a^{-1}) and a contribution to sea-level rise of ∼0.7 mm from 2000 to 2018. Glacier retreat is assumed to continue in the next decades. Rounce [8] projects a HMA glacier mass shrinkage between (29 ± 12) % (Representative Concentration Pathway 2.6) and (67 ± 10) % (Representative Concentration Pathway 8.5) for the period 2015 to 2100. The changes are caused by increased temperatures, changing precipitation amounts and changes in the ratio between liquid and solid precipitation (e.g., [9]). Wei and Fang [10] report a decadal warming rate of 0.32 K for the period 1961 to 2010. Nevertheless, due to heterogeneous topography, influence of large-scale circulation systems (e.g., [11–18])

and their interactions with local atmospheric circulation systems responses of glaciers largely vary in space (e.g., [19–22]). Winter-, spring- and summer-accumulation and mixed type glaciers can be found in HMA [23,24]. Summer-accumulation type glaciers are especially sensitive to changes in summer temperatures [25], e.g., due to snow–albedo feedback [26–28].

Changes in glacial lake patterns are a consequence of glacier change. These changes include the number of lakes, the lake area, the volume of glacier lakes and the spatial distribution of lakes. Wang et al. [29] have shown the correlation of decreasing glacier area and increasing number of lakes, with a peak in the elevations between 5500 and 6000 masl (see Figure 16, [29]) since the 1970s. With the increasing number of unstable glacier lakes and increasing water volume of existing lakes [30], the potential threat trough glacial lake outburst floods (GLOFs) (e.g., [31–33]) is increasing in the Hindu Kush Himalayas region and in particular in the Himalayas [34] and Nepal [35].

Due to the remoteness and harsh climate conditions in HMA, good documentation and in-situ analyses of GLOF are scarce. Halji village in northwestern Nepal [36] was affected by six GLOFs between 2004 and 2011 [37]. The village is located in Limi valley in the district Humla. Several buildings of the ∼400 inhabitants of the village were damaged [36,38], and as a result in 2010, a gabion wall was constructed to protect the village [38]. The wall was repaired after GLOF damage in 2011 and further extended in 2014 [38]. The source of the GLOFs is an ice-dammed basin located at the tongue of the Halji glacier (30.26° N, 81.47° E, see Figure 1), forming a potential glacier lake. The lake is drained by the Halji Khola (river) which flows through Halji Village. The linear distance between village (∼3800 m a. s. l.) and glacier (mean elevation 5500 m a. s. l.) is ∼6 km.

The region is located north of the Himalayan main ridge. It is influenced by the westerlies [11] and south Asian monsoon systems [39,40], particularly the Indian Summer Monsoon [19]. Westerlies dominate in winter [11]. With the northward shift of the westerlies during summer, the area is mainly influenced by the monsoon [11,19]. According to the glacier accumulation regime classification of (see Figure 14 in [24]), the region lies within the transition zone from mostly winter-accumulation type glaciers further to the west, to glaciers with summer-accumulation and mixed accumulation regimes in Nepalese regions to the east.

In this study, we statistically downscale the European Centre for Medium-Range Weather Forecasts (ECMWF) reanalysis ECMWF Reanalysis fifth generation-Land (ERA5-L) [41] to the location of an automatic weather station (AWS) installed in the immediate vicinity of the glacier. This 40 year dataset was used to create distributed climate data input fields to force the COupled Snowpack and Ice surface energy and mass balance model in PYthon (COSIPY) [42] to the Halji glacier. COSIPY model development and testing details are provided by Sauter et al. [42]. It is the main tool of this study. With the resulting glacier mass balance fields, we analyzed the dominating atmospheric drivers and their influence on the interannual variability of the glacier's mass budget. Moreover, simulations with temperature and precipitation perturbations were executed, and seasonal sensitivity characteristic after Oerlemans and Reichert [43] were calculated. The first method focuses on the impact of an overall change on the annual mass balance, while the latter refers to the impact on the annual mass balance from changes in individual months. Finally, to identify possible teleconnections, we investigated the monthly, seasonal and annual variability of the MB by correlating it with 22 different circulation and monsoon indices. The present study focuses on the atmospheric sensitivity of the Halji glacier in the transition zone between mainly monsoon influenced glaciers to the east and more westerly influenced glaciers to the west.

In Section 2, the Halji glacier is presented in more detail. The MB model, the AWS data, the applied downscaling procedure, the simulation setup and the applied sensitivity methods are described in Section 3. The results are presented in Section 4 and discussed in Section 5.

2. Halji Glacier

The Halji glacier extends between 5251 and 5658 m a. s. l. (mean: 5430 m a. s. l.) [44] with an area of 2.3 km^2 [45] in 2001. The glacier has an estimated maximum thickness of 83 m ([22], dataset: [46]) and an estimated mean flow velocity of 2.3 m a^{-1} ([47], dataset: [48]) (see Appendix A Figure A1).

Kropáček et al. [38] determined an annual geodetic MB of (-0.40 ± 0.30) m w.e. a^{-1} between 2000 and 2013. Shean et al. ([7], dataset: [49]) calculated an annual geodetic MB of (-0.70 ± 0.09) m w.e. a^{-1} between 2000 and 2018. Both studies use digital elevation model (DEM) differencing but for different periods. As reported by Ye et al. [50], the glaciers in the Naimona'nyi region (∼25 km northwest of Halji glacier) have retreated at least since 1976. The only information about the Halji glacier development pre-millennial are glacier outlines derived from satellite data and the resulting glacier areas as displayed in Figure 1. The glacier area decreased from 3.1 km^2 in 1974 [51] to 2.3 km^2 in 2001 [45]. Between 2001 and 2010, the area was relatively stable with still 2.2 km^2 in 2010 [52], but decreased to 1.9 km^2 by 2018. The 2018 outline was derived from a Sentinel 2 [53] scene found with the Google Earth Engine Digitisation Tool developed by Lea [54]. According to the outline of the Randolph Glacier Inventory 6.0 (RGI6) [45], the glacier has two ice divides (see green lines Figure 1). All other outlines have been adjusted to these divides.

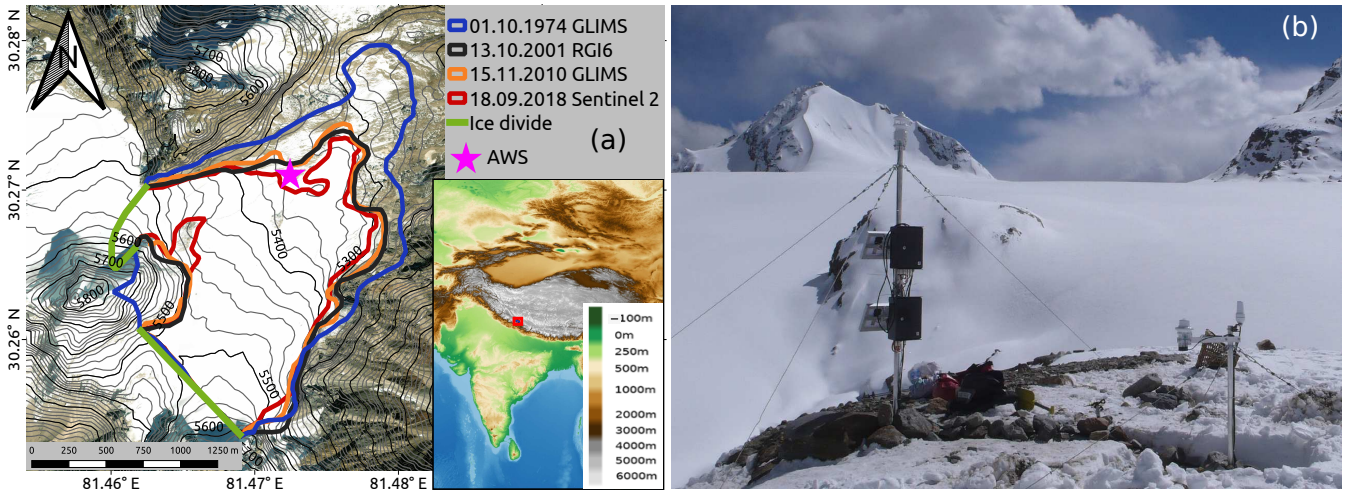

Figure 1. The Halji glacier with multi-temporal glacier outlines and satellite image map in the background [55] (**a**) and photo of the automatic weather station (AWS) of the Chair of Climatology (Technische Universität Berlin) installed in 2018 with a part of the glacier in the background (**b**, photo by Benjamin Schröter). Colors within the inset map represent elevation [56].

3. Data and Methods

In the following section, the applied physically-based surface energy and mass balance model COSIPY is described. Afterwards, the AWS and the meteorological forcing of COSIPY with the applied downscaling approaches are presented in Section 3.2. The setup for the simulations in this study is summarized in Section 3.3. The applied statistics, the seasonal sensitivity characteristic (SSC) and circulating and monsoon indexes are presented in Section 3.4. An overview of all introduced symbols and constants with their units can be found in Appendix A.

3.1. COSIPY

COSIPY is of medium complexity within the range of available surface energy balance (SEB) and MB models [42]. It is physically based and combines SEB processes with an adaptive (non-equidistant) subsurface scheme. The possibility of the identification of important atmospheric MB drivers, the easy implementation on High-Performance Computing Clusters (HPCCs) and the modular structure (maximum traceability) are some

of the key points focused on during the development of the model. The open-source model is written in Python 3. The source code is freely available on a git repository (https://github.com/cryotools/cosipy, accessed on 13 March 2021). We use version COSIPY v1.3 (https://doi.org/10.5281/zenodo.3902191, accessed on 13 March 2021) in the distributed setup. The temporal and spatial resolution of the simulations is scalable, depending on the temporal resolution of forcing variables and the spatial resolution of the applied DEM. The SEB is defined as the sum of all energy fluxes at the surface:

$$Q_M = Q_{SWin}(1-\alpha) + Q_{LWin} + Q_{LWout} + Q_H + Q_E + Q_G + Q_R \quad (1)$$

where Q_M is available melt energy, Q_{SWin} is incoming shortwave radiation, α is snow/ice albedo, Q_{LWin} is incoming longwave radiation, Q_{LWout} is outgoing longwave radiation, Q_H is sensible heat flux, Q_E is latent heat flux, Q_G is glacier heat flux and Q_R sensible heat flux of rain. Q_{SWin} and Q_{LWin} are input parameters of COSIPY whereby Q_{LWin} can be parametrized (see Equations (14) and (15), [42]). Cloud cover fraction is needed as input in the latter case. The decay of α is calculated after Oerlemans and Knap [57] with the parameters presented and studied by Mölg et al. [58] in HMA. All other terms on the right-hand side of Equation (1) depend on the surface temperature T_s. The resulting nonlinear equation is solved iteratively with an optimization algorithm. Due to physical constraints, $T_s \leq$ melting point temperature T_m must be fulfilled and therefore energy surplus results in $Q_M > 0$ when T_s equals T_m. If $T_s < T_m$, there is no available energy at the surface, i.e., $Q_M = 0$. All energy fluxes are of positive (negative) algebraic sign towards (directed away from) the surface and presented in W m^{-2}.

The SEB is linked through T_s as an upper Neumann boundary condition [59] to the heat equation of the subsurface module. Furthermore, surface melt and rain percolates through the snowpack and can result in refreezing within the snow layers. A small part of net shortwave radiation $Q_{SWnet} = Q_{SWin}(1-\alpha)$, penetrates the uppermost layers [60], warms these layers and result in subsurface melt, if the additional energy would otherwise result in inconsistent layer temperature $T_l > T_m$. Moreover, parametrizations for the densification of the snow [61,62] and the development of the snow/ice surface roughness [58] were implemented.

COSIPY is a one-dimensional point model that calculates in its distributed setup the MB at each point on the glacier and neglects exchange of lateral mass and energy transport. Processes at the base of the glacier are also neglected, which is why in the following, the simulated MB is referred to as the climatic mass balance b_{clim} in accordance with Cogley et al. [63]. It is the sum of mass changes through accumulation and ablation and therefore links climate variability to glacier-mass gain or loss [64]. It is calculated as follows [63]:

$$b_{clim} = c_{sfc} + a_{sfc} + c_i + a_i = b_{sfc} + b_i \quad (2)$$

where surface accumulation is c_{sfc}, surface ablation is a_{sfc}, internal accumulation is c_i, internal ablation is a_i, surface mass balance is b_{sfc} and internal mass balance is b_i. Accumulated snowfall SF_c and deposition (resublimation) of water vapor result in c_{sfc}. COSIPY does not consider direct sublimation during snowfall and processes associated with snowdrift. Therefore, frozen precipitation equals SF_c within COSIPY. Surface ablation consists of sublimation and surface melt resulting from Equation (1). Internal accumulation equals refreezing within the snowpack and a_i equals subsurface melt through penetrating radiation. Mass balance components are positive (negative) if they are a mass gain (loss) in m w.e. In accordance with Cogley et al. [63], a capital B denotes the glacier-wide MB (sum of all point balances) with the same suffixes than b. The annual climatic mass balance is $b_{clim,a}$. The cumulative climatic mass balance is $b_{clim,cum}$. When we refer to the mass-balance year (MB-year) of $b_{clim,a}$ and other variables, we speak of the hydrological year, starting after the approximated end of the preceding ablation season on 1 October and ending on 30 September of the following year, whereby the year of the included January is used as name of the MB-year in accordance with Cogley et al. [63]. For further information

on applied parametrizations, physical principles and technical infrastructure of COSIPY, please read Sauter et al. [42].

3.2. Climate Forcing Model Input

3.2.1. Automatic Weather Station Measurements

An AWS [65] was installed in December 2013 by the Chair of Climatology (Technische Universität Berlin) and was replaced by a new AWS in 2018 (see Figure 1). The AWS is located adjacent to the Halji glacier at an elevation of 5359 m a. s. l. The data are continuously transmitted via Iridium satellite telemetry to a server of the Chair of Climatology at Technische Universität Berlin, Germany. Observations from 20 April 2018 until 2 November 2019 are used to statistically downscale atmospheric reanalysis data. Due to technical problems with total precipitation measurements, the available period starts in that case on 2 August 2018. The measured variables, measuring instruments and nominal accuracies are summarized in Table 1.

Table 1. Variables, instruments, measuring range and nominal accuracies of the automatic weather station located at 5359 m a. s. l. in the direct vicinity of Halji glacier. The full name of the instruments are Lufft WS501-UMB Smart Weather Sensor and Lufft WS100 Radar Precipitation Sensor.

Variable	Instrument	Measuring Range	Nominal Accuracy
Surface pressure	Lufft WS501-UMB	300 … 1200 hPa	± 0.5 hPa (0 … 40 °C)
Air temperature at 2 m	Lufft WS501-UMB	–50 … 60 °C	± 0.2 °C (-20 … 50 °C), ± 0.5 °C (< -30 °C)
Total precipitation	Lufft WS100 Radar	0.01 … 200 mm h^{-1}	± 0.16 mm or ± 10 % *
Relative humidity at 2 m	Lufft WS501-UMB	0 … 100%	± 2 %
Wind speed at 2 m	Lufft WS501-UMB	0 … 75 m s^{-1}	± 3 % (0 … 35 m s^{-1}), ± 5 % (> 35 m s^{-1}) *RMS*

* for liquid precipitation.

Data of the first installed AWS from 1 December 2013 until 17 April 2018 were additionally used to evaluate downscaled surface pressure p_{sfc}, air temperature at 2 m T_2 and relative humidity at 2 m RH_2.

3.2.2. Downscaling ERA5-L

Required COSIPY forcing variables are derived from the atmospheric reanalyses ERA5-L produced by ECMWF within the Copernicus Climate Change Service. ERA5-L—a subversion of ERA5—provides ERA5 surface variables on a ∼9 km grid, instead of the original ∼31 km ERA5 grid. After producing ERA5, the Hydrology revised Tiled ECMWF Scheme for Surface Exchanges over Land (H-TESSEL) of the ERA5 integrated forecast system (IFS CY41R2) was re-executed with spatially interpolated (to a 9 km grid) ERA5 variables to produce ERA5-L [66]. Air temperature at 2 m T_2 and dewpoint temperature at 2 m $T_{d,2}$ are the only COSIPY forcing variables that contain new information in comparison to ERA5. All other variables are also H-TESSEL forcing variables and therefore contain no new information [41,66,67]. We used hourly data from January 1981 until April 2020 from the grid cell, which represents the area between 30.25° N, 81.45° E and 30.35° N, 81.55° E. Halji glacier lies completely within this grid cell. ERA5-L data can be downloaded free of charge from the climate data store (https://cds.climate.copernicus.eu/cdsapp#!/dataset/reanalysis-era5-land?tab=form, accessed on 12 December 2020).

The preprocessing steps to start COSIPY simulations can be divided into two steps. An overview of the applied approaches is provided in Table 2. First, we downscale the ERA5-L data to the location of the installed AWS at the glacier. Second, the downscaled forcing variables at the location of the AWS are interpolated with a DEM to the applied distributed fields on the glacier. The used ERA5-L grid cell has a model elevation of 5154 m a. s. l., which lies 205 m below the elevation of the AWS.

Table 2. COupled Snowpack and Ice surface energy and mass balance model in PYthon (COSIPY) forcing variables with required units, applied downscaling approaches to ERA5-L data and approaches to create the distributed fields (interpolation) on the glacier. The second column denotes if the variable is also measured by the automatic weather station (AWS). A dash stands for no downscaling.

Variable	AWS	Downscaling	Interpolation
Surface pressure p_{sfc} (hPa)	yes	Barometric formula	Barometric formula
Air temperature at 2 m T_2 (K)	yes	Quantile mapping	Lapse rate
Relative humidity at 2 m RH_2 (%)	yes	Lapse rate	-
Incoming shortwave radiation Q_{SWin} (W m^{-2})	yes	-	Radiation modelling [68]
Incoming longwave radiation Q_{LWin} (W m^{-2})	no	-	-
Wind speed at 2 m U_2 (m s^{-1})	yes	Scale factor of 5	-
Total precipitation TP (mm)	yes	Scale factor of 2	-

For surface pressure p_{sfc}, we apply the barometric formula for both the downscaling to the elevation of the AWS and the interpolation to the distributed fields [69]:

$$p_{sfc} = p_0(1 - \frac{a}{T_0}h)^{\frac{Mg}{aR}} \quad (3)$$

where p_0 is atmospheric pressure at reference height, a thermal gradient, T_0 air temperature at reference height, h height difference, M average molar mass of air, g gravitational acceleration and R gas constant (see Appendix List of constants).

We observed that the seasonal amplitude of ERA5-L's T_2 is greater than the measured T_2, resulting in a warm bias of temperature in summer and a cold bias in winter temperature. Therefore, we applied a quantile-mapping approach [70] to downscale the data to the AWS. For generation of the distributed T_2 fields, we use a lapse rate of −0.6 K (100 m)$^{-1}$. The lapse rate is calculated from the long-term mean (1981 to 2019) of T_2 of 121 ERA5-L grid cells around Halji glacier (see Appendix A Figure A2).

Derived ERA5-L relative humidity at 2 m RH_2 is calculated from saturation water vapor of T_2 and $T_{d,2}$ (see [71,72]). We use a constant value for all glacier grid points (GGPs) for the distributed RH_2 fields on the glacier. For the two radiation components Q_{SWin} and Q_{LWin} we do not use downscaling from raw ERA5-L to the location of the AWS. However, a radiation model after Wohlfahrt et al. [68] is used to calculate the distributed input fields of Q_{SWin} on the glacier. The model takes slope, aspect, timestamp, latitude, longitude of the GGPs and Q_{SWin} of ERA5-L as input and calculates Q_{SWin} for each GGPs. Q_{LWin} is taken constant in space for all GGPs without interpolation. To derive wind speed at 2 m U_2, first wind speed at 10 m U_{10} has to be calculated from u and v component of 10 m wind, which is described on the ERA5 website (https://confluence.ecmwf.int/pages/viewpage.action?pageId=133262398, last access: 12 December 2020). Afterwards, we use the logarithmic wind profile to calculate U_2 [73]:

$$U_2 = U_{10}\frac{\ln\frac{2}{z_0}}{\ln\frac{10}{z_0}} \quad (4)$$

where z_0 is surface roughness. We use a value of 2.12 mm for z_0, which is the mean between the upper and lower boundary condition (firn: 4 mm [74] and fresh snow: 0.24 mm [75]) in the surface roughness parametrizations of COSIPY. We use a constant value for all GGPs for distributed U_2 fields on the glacier.

3.2.3. Comparison of Downscaled ERA5-L to Automatic Weather Station Measurements

Figure 2 presents the comparison between measured and ERA5-L downscaled variables p_{sfc}, T_2 and specific humidity at 2 m SH_2. For comparison, we use SH_2 instead of RH_2, the forcing variable required by COSIPY, to exclude differences that are solely based on differences in T_2 and p_{sfc}. The course of the year of all three measured variables can be reproduced by ERA5-L, which is displayed in the left panels. This is supported by

the scatterplots in the middle panels and the statistics of the applied linear least-square regression with all coefficients of determination $r^2 \geq 0.9$ (p_{sfc}: 0.99, T_2: 0.90, SH_2: 0.93), small root mean square errors (RMSE, p_{sfc}: 0.5 hPa, T_2: 2.3 K, SH_2: 0.7 g kg^{-1}), small mean bias errors (MBE, p_{sfc}: 0.18 hPa, T_2: <0.01 K, SH_2: 0.03 g kg^{-1}) and regression line slopes close to 1 (p_{sfc}: 1.1, T_2: 0.94, SH_2: 1.18). All results are statistically significant with p-value < 0.01. The cumulative distribution functions in the right panels reveal that the downscaling approach in case of p_{sfc} and T_2 result in a substantially improved agreement with AWS measurements. A decrease in MBE from 14.3 to 0.2 hPa (RMSE: from 14.3 to 0.5 hPa) in case of p_{sfc} and from 0.14 to <0.01 K (RMSE: from 3.4 to 2.3 K) in case of T_2 could be achieved. In case of SH_2, almost no improvement (MBE: 0.05 to 0.03 g kg^{-1}) can be observed. The reason might be that RH_2 mean of the measured values and the corresponding raw ERA5-L values differ only by 0.3 % (Measured: 77.1 %, ERA5-L: 76.8 %).

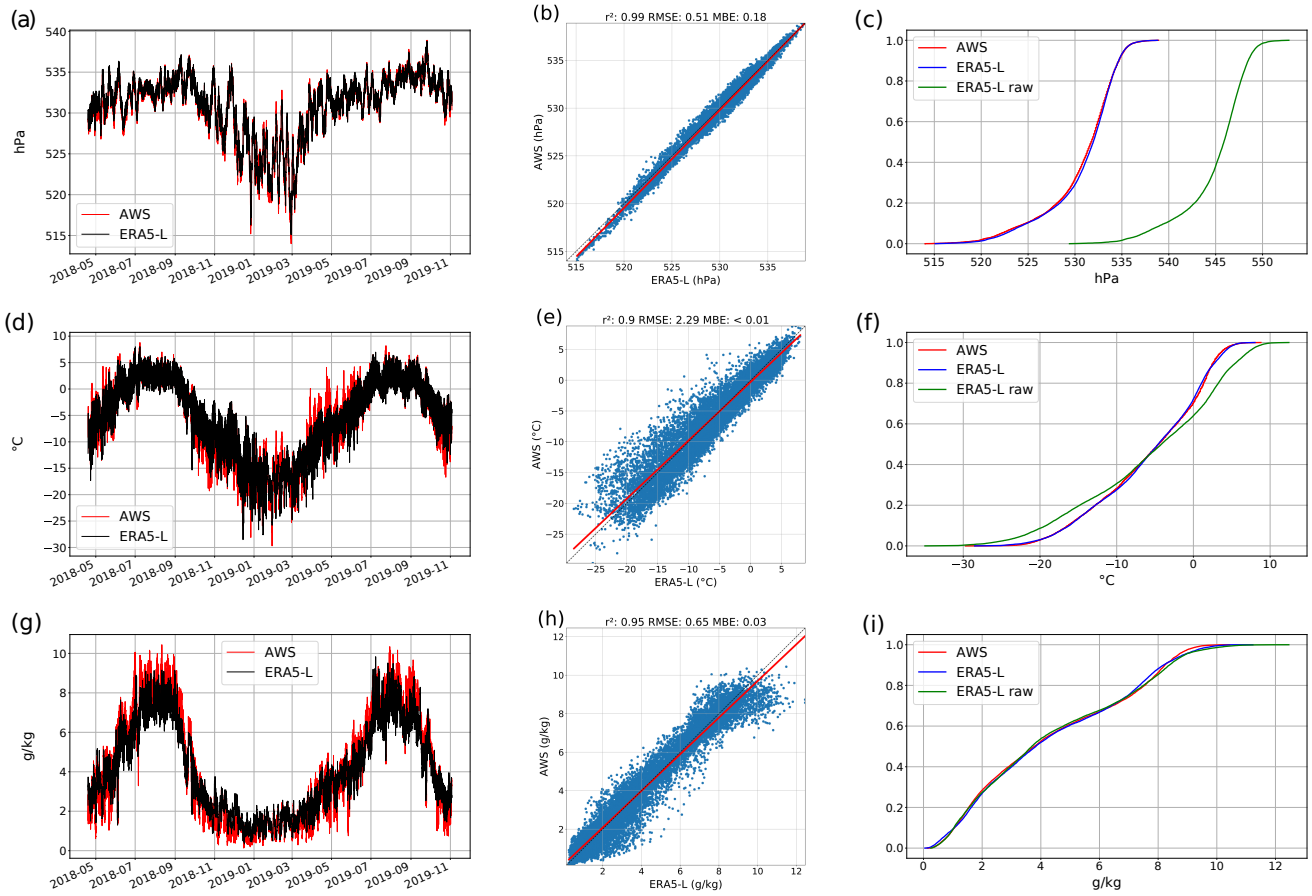

Figure 2. Comparison between measurements of the automatic weather station (May 2018–October 2019) and the downscaled European Centre for Medium-Range Weather Forecasts (ECMWF) Reanalysis fifth generation-Land (ERA5-L) variables air pressure (**a**–**c**), air temperature at 2 m (**d**–**f**) and specific humidity (**g**–**i**) at the location of the automatic weather station. The time series are presented in the left panels (**a**,**d**,**g**), the scatterplots in the middle panels (**b**,**e**,**h**) and the cumulative distribution functions in the right panels (**c**,**f**,**i**). A linear least-square regression model is used for the scatterplots, where the red line shows the regression line. ERA5-L-raw denotes the unscaled ERA5-L variables. In all plots, hourly values are displayed.

As mentioned in Section 2, we additionally compared p_{sfc}, T_2 and SH_2 with measurements of the earlier installed AWS between 1 December 2013 and 17 April 2018. Due to measurement gaps, 65 % of p_{sfc} and 26 % of T_2 and SH_2 values could be used. The calculated r^2 of the linear least-square regression are again all > 0.9 (p_{sfc}: 0.98, T_2: 0.92, SH_2:

0.92), the RMSEs are within a tolerable range (p_{sfc}: 4.4 hPa, T_2: 2.4 K, SH_2: 1.0 g kg^{-1}) and regression line slopes are acceptable (p_{sfc}: 1.05, T_2: 0.94, SH_2: 0.76).

We observed a distinct difference when comparing ERA5-L U_2 and measured U_2. The hourly mean of measured U_2 is 5 times the ERA5 U_2. Hourly values of U_2 are compared in Figure 3. Figure 3a shows the difference when comparing the data. It was not possible to apply a complex wind modeling approach within the scope of this study, also because of the lack of a highly resolved DEM. Therefore, we applied a scale factor of 5 to ERA5-L U_2, which is presented in Figure 3b. The cumulative distribution function in Figure 3c reveals the improvement in the distribution of scaled ERA5-L U_2 data in comparison with measured data. This is supported by the decrease of the MBE from 3.74 to < 0.01 m s^{-1}.

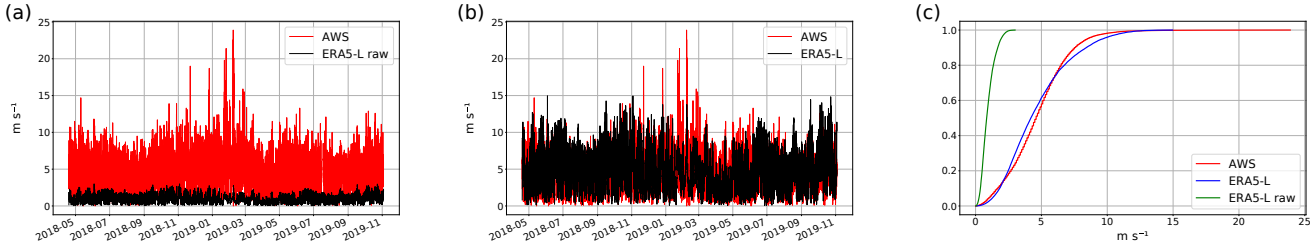

Figure 3. Measured (AWS) and ERA5-L wind speed at 2 m. Time series without wind scaling (**a**, ERA5-L-raw), with wind scaling (**b**, ERA5-L), and the cumulative distribution functions (**c**) with unscaled and scaled ERA5-L wind speed at 2 m. In all plots hourly values are displayed.

In the period from August 2018 to November 2019, measured total precipitation TP was twice the amount of ERA5-L TP. We used this as a scale factor (Figure 4). The scaling results in a decrease of MBE from 0.12 mm to 0.02 mm h^{-1}.

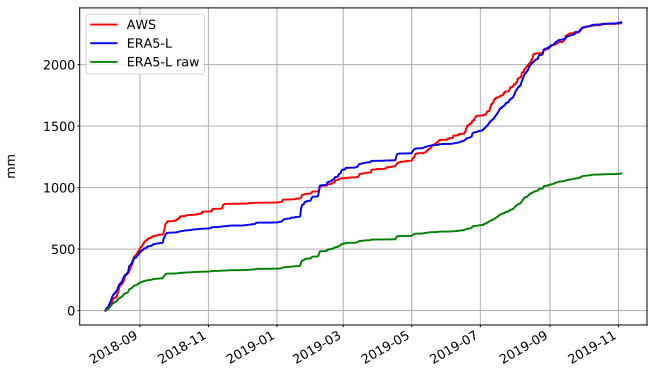

Figure 4. Cumulative measured (AWS), unscaled (ERA5-L-raw) and scaled (ERA5-L) hourly total precipitation from 2 August 2018 to 2 November 2019.

3.3. COSIPY Simulations

As static data, a glacier outline and DEM are required to start COSIPY simulations in the distributed setup. We used a time-invariant reference outline from RGI6 [45] (see Figure 1) for the simulation period October 1981–September 2019. Further, we used the 1 arcsecond global product [44] of the Shuttle Radar Topography Mission (SRTM) as DEM. With the elevation information of all GGPs, we used the Geospatial Data Abstraction Library (GDAL) [76] to calculate all slopes and aspects of the GGPs needed as input for the radiation module of Wohlfahrt et al. [68]. Furthermore, we aggregated the DEM with GDAL to spatial resolutions between ∼30 and ∼1500 m. The applied spatial resolutions in arcseconds and ∼m and the number of resulting GGP is summarized in Table 3.

Table 3. Applied spatial resolutions and resulting glacier grid points (GGPs) for the Halji glacier. Not all applied resolutions are shown.

Resolution in arcseconds (″)	**1.0**	**2.0**	**3.0**	**3.33**	**5.0**	**6.67**	**10.00**	**16.67**	**30.0**	**33.33**	**50.0**
Resolution in ∼m	30	60	90	100	150	200	300	500	900	1000	1500
Resulting GGPs	2735	688	303	248	110	59	28	11	4	2	1

We created the distributed COSIPY input fields and started simulations for the whole available ERA5-L period from January 1981 to April 2020 at an hourly resolution for all spatial resolutions. We then calculated annual deviations of $B_{clim,a}$ to the 30 m resolution simulation in order to identify the best trade-off between computational power and reasonable results. The deviations are presented in Figure 5.

All deviations until the resolution of ∼100 m are within a tolerable range (±0.02 m w.e. a^{-1}). Therefore, for all further simulations in this study, we used a spatial resolution of ∼100 m with the resulting 248 GGPs representing the entire Halji glacier. For all distributed simulations, we used the HPCC of the Climate Geography lab of Humboldt-Universität zu Berlin, Germany. A simulation with ∼100 m resolution and 248 GGPs has a runtime of less than two hours for the whole ERA5-L period from January 1981 to April 2020.

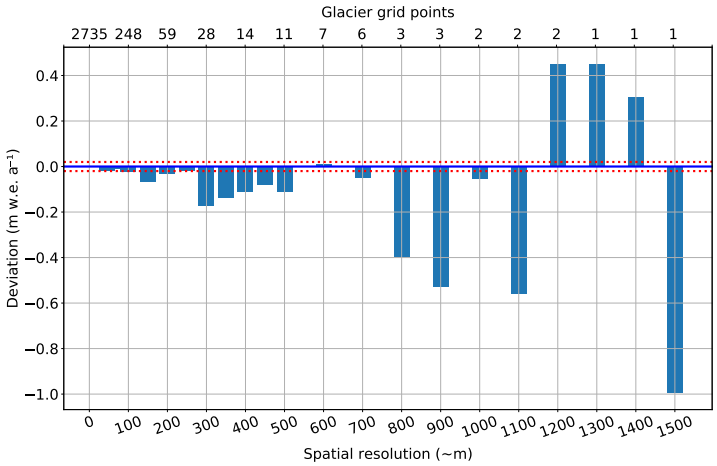

Figure 5. Deviations of the mean annual glacier-wide climatic mass balance of the Halji glacier to the reference 30 m simulation for the mass-balance years (MB-years) 1982 to 2019 for different spatial resolutions ranging from 60 to 1500 m. Corresponding glacier grid points are on the second x-axis. The red dotted lines showing the selected threshold for deviations in a tolerable range (±0.02 m w.e. a^{-1}).

3.4. Sensitivity Studies and Large Scale Teleconnections

Statistics: To investigate the influence of the forcing variables on the interannual variability of $B_{clim,a}$, we calculate non-parametric Spearman's rank correlation coefficients r_s [77] between $B_{clim,a}$ and the different forcing variables and the intermediate variables Q_{SWnet}, α and net longwave radiation Q_{LWnet}. We define two significance levels with a 95 % and 99 % confidence interval and access the significance with the two-sided p-value of the Spearman's rank correlation [77]. Furthermore, we start simulations with ±0.5, ±1.0, ±2.0 K T_2 and ±5, ±10, ±20 % TP perturbations and analyzed the resulting annual deviations of $B_{clim,a}$ to the original run.

Seasonal Sensitivity Characteristic (SSC): Oerlemans and Reichert [43] proposed calculating SSC to describe the dependency of B_{clim} of a glacier to the local seasonal climate in a uniform and structured manner. The SSC of a glacier is a 2 × 12 matrix quantifying the B_{clim} sensitivity to temperature and precipitation perturbations each in the 12 months of the year. For their calculation in the first step, the reference COSIPY simulation was

adjusted so that the mean $B_{clim,a}$ is zero. Therefore, the mean forcing temperature is adjusted in the range of ±2 K. For the Halji glacier, we applied a T_2 offset of −0.37 K (see Appendix A Figure A3) to arrive at a zero $B_{clim,a}$ for the period October 1981–September 2019. In the second step, 24 COSIPY simulations were forced with monthly T_2 perturbations of ±0.5 K and 24 COSIPY simulations were forced with monthly TP perturbations of ±10 %. The resulting differences of $B_{clim,a}$ between the positive and negative perturbation for each month are the 12 temperature values and the 12 precipitation values of the SSC. These 24 values are displayed as a bar plot. For further information, including the equations of the concept, please see Section 2, especially Equations (3) and (4) in Oerlemans and Reichert [43] and Section 3b in Reichert et al. [78].

Indexes: Finally, we calculate r_s between $B_{clim,a}$ and 22 common teleconnection indexes. The temporal resolution and coverage, short and long name, reference and download location of the indexes are summarized in Table A1 in the Appendix A. In doing so, we test the relationship between COSIPY-simulated Halji glacier B_{clim} and atmospheric drivers.

4. Results

The $B_{clim,a}$ for MB-years 1982 to 2019 of Halji glacier and the corresponding $B_{clim,cum}$ (1 October 1981 to 30 September 2019) are displayed in Figure 6. The mean $B_{clim,a}$ is −0.48 m w.e. a^{-1} and $B_{clim,cum}$ is −18.3 m w.e. The most negative annual balance is −2.16 m w.e. a^{-1} in 1990. The most positive is 0.57 m w.e. a^{-1} in 2013. The overall standard deviation of 0.71 m w.e. a^{-1} reflects the quantitative interannual varability in the mass balance time series. Between 1995 and 2007 all Halji glacier annual mass balances are negative (mean −0.53 m w.e. a^{-1}). In contrast, between 2008 and 2015, the glacier balance was in equilibrium (only two negative MB-years 2012 and 2014) with a mean $B_{clim,a}$ of 0.0 m w.e. a^{-1} over this period (see Figure 6b).

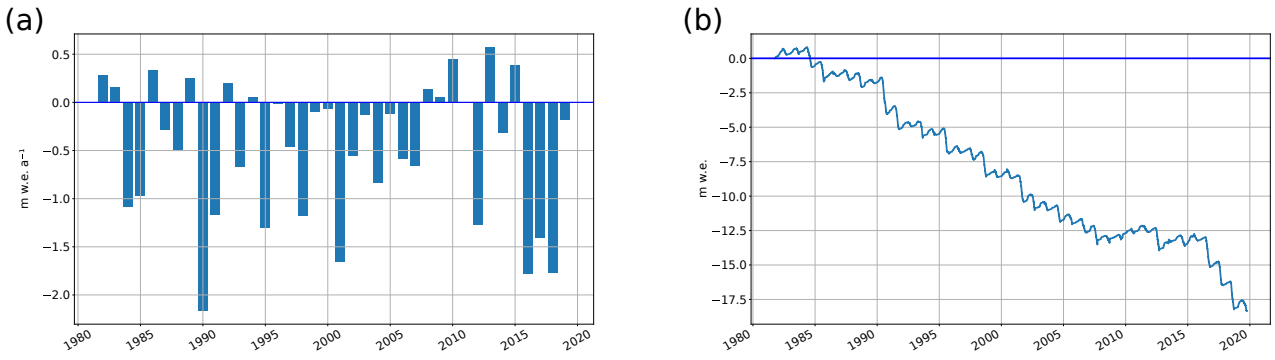

Figure 6. Simulated annual glacier-wide climatic mass balance (**a**) and cumulative (**b**) glacier-wide climatic mass balance of the Halji glacier from 1982 to 2019.

4.1. Sensitivity to Climate Forcing Input Variables

Table 4 displays the non-parametric Spearman's rank correlation coefficient r_s between $B_{clim,a}$ and the forcing variables as well as four intermediate (SF_c, Q_{SWnet}, Q_{LWnet} and α) variables.

On annual basis the forcing variables T_2, U_2 and TP have the highest correlation with all $r_s > 0.4$. Whereby, T_2 and U_2 by themselves are highly significantly correlated with an annual r_s of 0.69 (not displayed in Table 4, p-value < 0.01). No significant annual correlation could be found between T_2 and TP, and U_2 and TP.

Table 4. Spearman's rank correlation coefficients between monthly forcing (f) and intermediate (i) variables and annual glacier-wide climatic mass balance. Grey coefficients are not significant, normal font denotes significance level 0.05 and bold and italic fonts significance level 0.01. The aggregation metrics to calculate annual and monthly values are displayed in the second row.

Variable	T_2	p_{sfc}	RH_2	U_2	TP	SF_c	Q_{SWin}	Q_{SWnet}	Q_{LWin}	Q_{LWnet}	α
Metric	mean	mean	mean	mean	sum	sum	mean	mean	mean	mean	mean
Type	f	f	f	f	f	i	f	i	f	i	i
Annual	***–0.42***	–0.07	0.36	***–0.45***	***0.42***	***0.54***	0.17	***–0.81***	–0.32	0.09	***0.8***
September before	–0.31	–0.09	0.26	–0.28	***0.43***	***0.47***	–0.15	–0.16	0.04	0.14	0.14
October	***–0.49***	–0.3	***0.43***	–0.21	0.36	0.36	–0.0	***–0.44***	–0.05	0.32	***0.44***
November	–0.32	–0.16	0.32	–0.37	–0.06	0.08	0.21	–0.37	–0.04	0.28	0.37
December	–0.06	–0.02	0.19	–0.17	0.16	0.19	–0.03	–0.14	0.1	0.13	0.14
January	–0.21	0.06	–0.11	0.18	0.33	0.29	0.0	–0.08	–0.0	0.06	0.09
February	***–0.55***	–0.2	–0.09	–0.2	0.18	0.24	0.05	–0.01	–0.35	–0.07	0.05
March	0.13	0.17	0.21	0.06	–0.15	–0.23	0.02	0.2	0.11	0.04	–0.21
April	–0.12	–0.04	–0.05	–0.08	0.04	0.12	0.16	–0.03	–0.17	–0.08	0.04
May	–0.39	–0.31	0.09	–0.06	0.03	0.0	0.25	–0.02	–0.36	–0.24	0.08
June	***–0.68***	–0.19	***0.51***	***–0.55***	0.03	0.35	0.22	–0.27	–0.36	–0.24	0.31
July	***–0.46***	0.16	0.04	–0.26	0.12	0.32	0.14	***–0.82***	–0.16	–0.12	***0.86***
August	–0.3	0.01	0.13	–0.37	0.11	0.31	–0.11	***–0.9***	–0.0	0.01	***0.91***
September	0.02	–0.17	0.01	–0.15	0.06	–0.02	–0.12	***–0.74***	0.01	0.14	***0.75***

On a monthly basis, the October temperature at the beginning of the MB-year and the February, June and July temperature mainly determine the interannual $B_{clim,a}$ variability. Interestingly, the monthly sum of TP in September before the MB-year starts explains the interannual variability with $r_s = 0.43$ (p-value < 0.01). The high statistical significance between RH_2 in June and $B_{clim,a}$ results to some degree from the correlation ($r_s = -0.37$, p-value < 0.05, not displayed in Table 4) between T_2 and RH_2. A statistically significant correlation of B_{clim} and the forcing variables p_{sfc} and Q_{SWin} could be found neither on annual nor monthly time scales. However, a significant correlation (p-value < 0.05) with the monthly mean of Q_{LWin} in February, May and June is present. Whereby, T_2 and Q_{LWin} are by themselves highly significant correlated in February ($r_s = 0.47$, p-value < 0.01), May ($r_s = 0.74$, p-value < 0.01) and June ($r_s = 0.82$, p-value < 0.01). The intermediate variables SF_c, Q_{SWnet} and α are superior in explaining interannual MB variability. The annual SF_c is mainly a result of the TP and T_2 variability. The interannual variance of α is the dominating driver ($r_s = 0.8$, p-value < 0.01) of the B_{clim} long-term variability. The correlation of Q_{SWnet} is in the same range because Q_{SWnet} and α are the strongest coupled variables with an annual r_s of 0.98 (not displayed in Table 4, p-value < 0.01).

The monthly deviations in percent (absolute values in Appendix A Figure A5) of $B_{clim,a}$, α, T_2, SF_c, Q_{SWin} and Q_{LWin} to their long-term monthly mean from 1982 to 2019 are shown in Figure 7. Deviations that are positive for $B_{clim,a}$ are blue, deviations with negative influence are red. $B_{clim,a}$ deviations are most pronounced in summer from May/June until September/October. In the case of T_2, it is roughly the opposite: the biggest deviations occur from October until May or June. Especially in July, August and September, there is a clear similarity in the patterns of the monthly $B_{clim,a}$ and α variability. The variability of SF_c is spread over the whole year, with two phases with low deviations in November and December and April and May. Monthly Q_{SWin} deviations from October to April/May are mostly negative from 1982 until 2003/2004 while being mostly positive compared to their long-term monthly mean. From June to September, Q_{SWin} and all monthly Q_{LWin} deviations do not show any clear pattern.

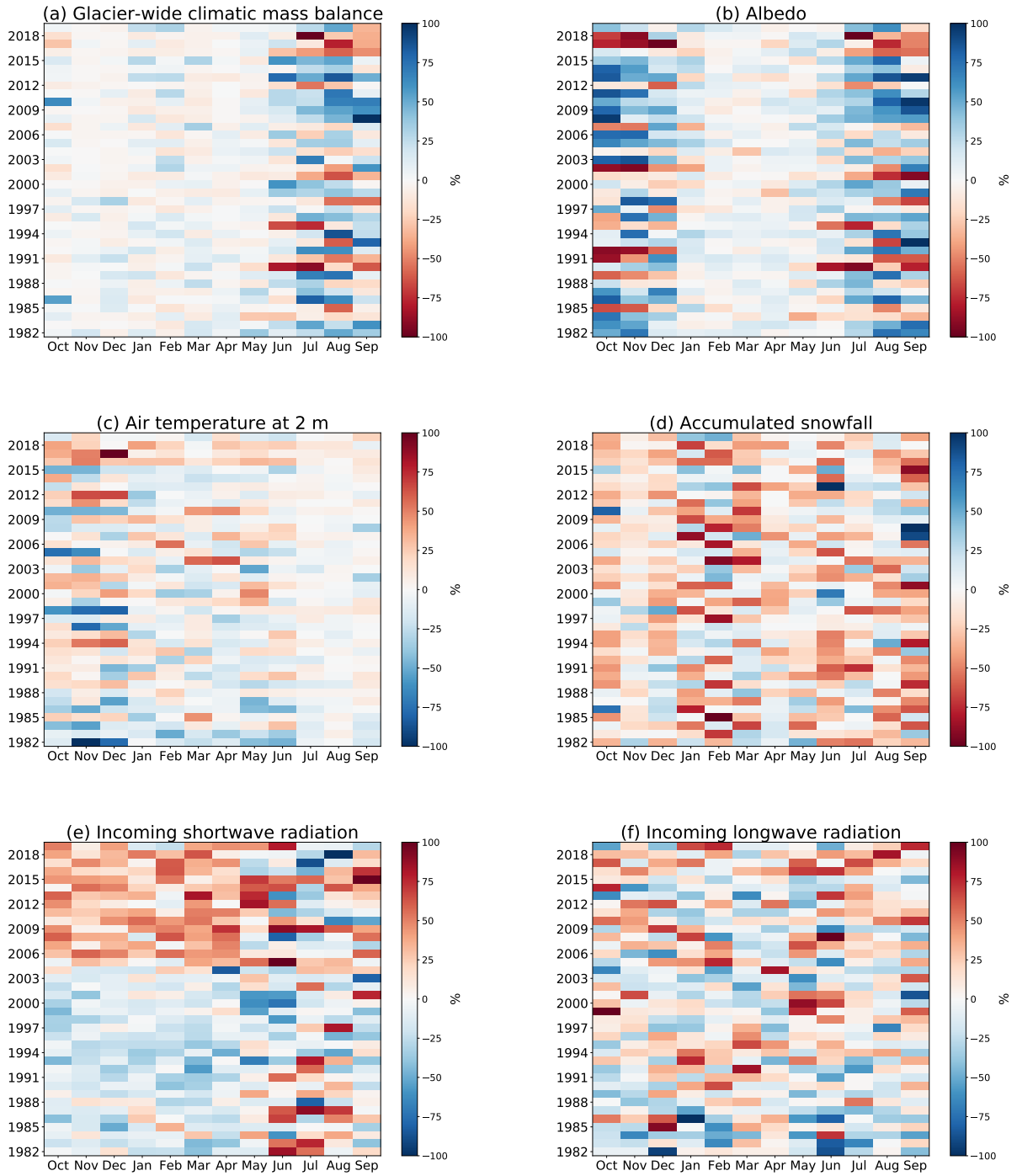

Figure 7. Monthly mean deviations 1982 to 2019 from long-term monthly mean values in percent (±100 % is maximum and minimum deviation) of glacier-wide climatic mass balance (**a**), albedo (**b**), air temperature at 2 m (**c**), accumulated snowfall (**d**), incoming shortwave radiation (**e**) and incoming longwave radiation (**f**). The color bar is arranged so that deviations that act positively (negatively) on glacier-wide climatic mass balance are shown in blue (red).

4.2. Temperature and Total Precipitation Perturbations and Seasonal Sensitivity Characteristic

Figure 8 shows the resulting $B_{clim,a}$ deviations of simulations with overall T_2 and TP perturbations. The results clearly show the nonlinear $B_{clim,a}$ responses to positive and negative perturbations. A T_2 perturbation of ±0.5 K results in a response roughly in the same range (−0.75 and 0.62 m w.e. a^{-1}). In contrast, a T_2 perturbation of ±2 K results

in a disproportionate mass response (−2.55 and 1.31 m w.e. a^{-1}). The same holds true in case of TP perturbations. A yearly positive response of 0.25 m w.e. a^{-1} and a negative of −0.29 m w.e. a^{-1} with a ±5 % TP change and a response of 0.76 and −1.29 m w.e. a^{-1} with ±20 % perturbation are found.

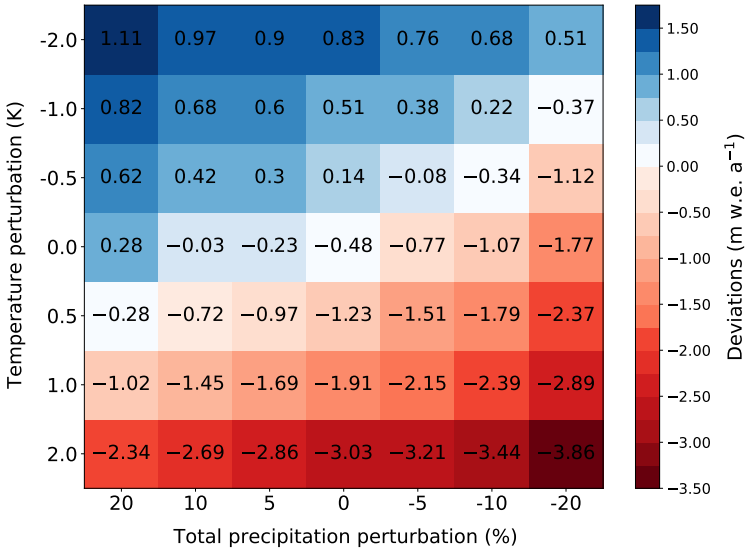

Figure 8. Mean (1982–2019) annual glacier-wide climatic mass balance (m w.e. a^{-1}) deviations from reference run ($B_{clim,a}$ = −0.48 m w.e. a^{-1}) for different overall temperature and total precipitation perturbations. The values within each pixel displays the actual mean $B_{clim,a}$ of the corresponding perturbation simulation. Please note that the color bar of the deviations is not centered around zero, reflecting the nonlinear response to same positive and negative perturbations.

Figure 9 displays the SSC after Oerlemans and Reichert [43]. The $B_{clim,a}$ sensitivity to T_2 is dominated by the months June to August and partly September. The peak in summer is also visible in $B_{clim,a}$ sensitivity to monthly TP perturbations while it is not that pronounced as the T_2 sensitivity. The $B_{clim,a}$ sensitivity to November TP perturbations is the lowest. $B_{clim,a}$ is for both T_2 and TP most sensitive to July perturbations. The sum of the T_2 response to July and August is significantly greater than the response to all other months combined. In the case of TP, it is the sum of the response to July, August and September, which is greater than the sum of the response to all other months combined.

4.3. Index Correlations

As presented in Section 3.4, we analyzed the response of $B_{clim,a}$ to 22 circulation and monsoon indices. Analogous to the forcing variables, we calculated the non-parametric r_s between $B_{clim,a}$ and the indices. With exception of the Webster and Yang Monsoon index (WYM) and the Polar/Eurasia index (POL), no significant correlations could be found with any of the indexes. Figure 10 displays $B_{clim,a}$ and the two indexes (annual values) that show significant correlations (p-value < 0.05) with $B_{clim,a}$. The WYM is calculated from the zonal wind shear between 850 and 200 hPa [79] between 0° and 20° N and 40° and 110° E. It is a broad-scale monsoon index differentiating between strong and weak monsoon seasons [79].

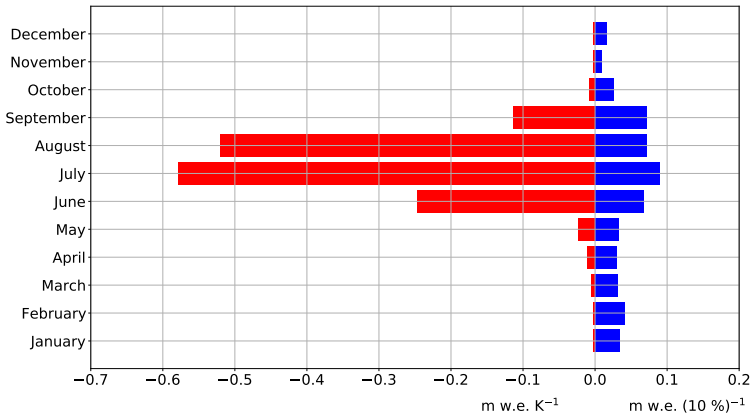

Figure 9. Seasonal sensitivity characteristic (SSC) after Oerlemans and Reichert [43]. Red bars are the dependence of annual glacier-wide climatic mass balance $B_{clim,a}$ on monthly temperature perturbations of 1 K and blue the dependence of $B_{clim,a}$ on monthly total precipitation perturbation of 10 %.

The POL links the Arctic polar vortex activity and mid-latitude circulation over the Asian continent [80,81] and is one of three modes describing anomalies that are derived from orthogonally rotated component analysis of the geopotential height at 700 hPa north of 15° N in the northern hemisphere [82,83]. The annual r_s (see Table 5) is 0.48 (p-value < 0.01) with POL and −0.42 (p-value < 0.05) with WYM. On a monthly bases, the highest values could be found between June values of POL and $B_{clim,a}$ with $r_s = 0.56$ (p-value < 0.01) and February with $r_s = 0.41$ (p-value < 0.05). The highest correlation of the seasonal index WYM and $B_{clim,a}$ is the combined June, July and August value with a r_s of –0.44 (p-value < 0.01).

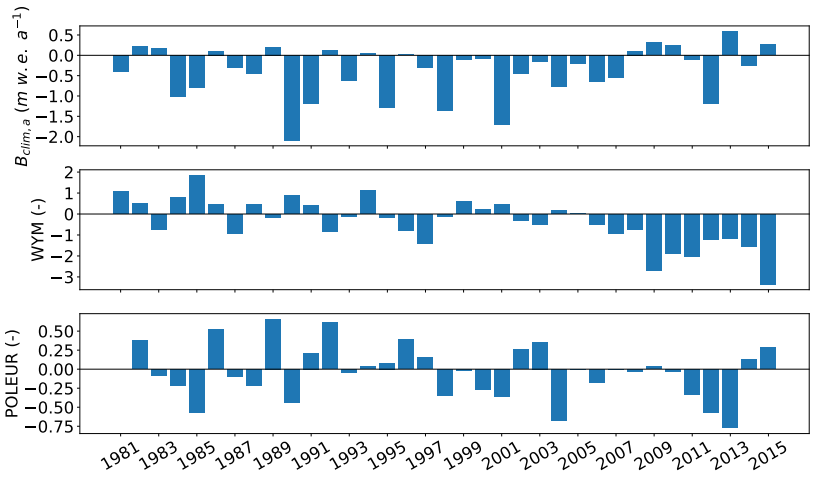

Figure 10. Annual glacier-wide climatic mass balance (1982-2015) of the Halji glacier (upper panel), Webster and Yang Monsoon index (WYM, middle panel) and Polar/Eurasia index (POL, lower panel).

Table 5. Spearman's rank correlation coefficient between the annual glacier-wide climatic mass balance and the Polar/Eurasia index (POL) and the Webster and Yang Monsoon index (WYM). Empty cells mark months or seasons when the index does not exist. Grey coefficients are not significant, normal font denotes significance level 0.05 and bold and italic fonts significance level 0.01.

Index	Annual	Jan	Feb	Mar	Apr	May	Jun	Jul	Aug	Sep	JJA	JJA
POL	***0.48***	0.29	0.41	–0.03	–0.05	–0.22	***0.56***	0.23	0.06	0.17		
WYM	–0.42						–0.43	–0.35	–0.33	–0.17	***–0.44***	–0.43

5. Discussion

5.1. Uncertainties

Model uncertainties can be separated in uncertainties stemming from forcing variables and uncertainties from the model itself.

5.1.1. Forcing Data Uncertainties

The statistical downscaling of the variables p_{sfc}, T_2 and RH_2 to the elevation of the AWS could be realised to a high degree of precision. The AWS is not located on the glacier and can therefore not account for possible T_2 dampening through melting glacier surface (e.g., [84]). With the current setup, we cannot assess this effect. At an elevation of 5350 m a. s. l. the area around the AWS is temporally snow-covered even in summer and therefore T_2 can be damped as well. The lower summer AWS T_2 values compared to ERA5-L T_2 might be related to this effect. In the case of U_2, the comparison between the ERA5-L and AWS values revealed a large difference. We scaled ERA5 U_2 to the location of the AWS. When it comes to local wind patterns, the location of the AWS is not representative for the whole glacier and affected by small scale features. Without a highly resolved DEM, we cannot achieve a better representation of U_2. We have planned to implement a snowdrift scheme (e.g., [85]) to account for effects of drifting and blowing snow in future studies. The effects are redistribution of snow, changed albedo patterns, direct sublimation of drifting and blowing snow and modified vertical temperature and moisture profiles [85,86]. This will require highly resolved wind fields that can be used to improve the U_2 representation. With the current setup, it is not possible to access the uncertainties of Q_{LWin}. We used the radiation model after Wohlfahrt et al. [68] for the generation of the distributed Q_{SWin} fields, which corrects the input fields, mainly dependent on slope and aspect of the GGPs. Olson and Rupper [87] and Olson et al. [88] have shown that radiation modeling is most important for valley glaciers with steep surrounding terrain, for steep glaciers with high elevation differences and glaciers at high latitudes. The Halji glacier located at low latitude contradicts all these conditions as a relatively flat glacier with uninterrupted skyline. Therefore, the influence of the radiation modeling is assumed to be of minor importance.

As described in Section 3.2.2 TP from ERA5-L does not contain any new information in comparison with TP from ERA5. Taking TP from an atmospheric dataset with ∼31 km spatial resolution results in the largest uncertainty when it comes to the forcing variables especially in alpine regions with complex terrain and at high evaluations above 5000 m a. s. l. (e.g., [89–92]). Immerzeel et al. [91] used an inverse approach to find the amount of precipitation, which is needed to sustain the measured glacier MBs. Precipitation in extreme cases in the upper Indus basin is assumed to be up to ten times higher than previously assumed according to their results. We scaled ERA5-L TP to the cumulative sum of measured TP by the AWS. We applied a constant scale factor of two to the ERA5-L data. After applying the scale factor, the timing of ERA5-L TP follows measured TP with some differences (see Figure 4). In follow-up studies, spatially higher-resolved atmospheric datasets (e.g., the High Asia Refined analysis version 2-2 m [92,93]) should be used to reduce uncertainties stemming from TP.

The applied DEM and its resolution have an influence on the model results as well. The first reason is the influence on the radiation module [87,94]. Furthermore, the coarser

the resolution, the less the resulting GGPs are representative for the different elevation ranges of the glacier. This is the reason for large and unsystematic deviations of resolutions with less than 30 GGPs (∼300 m) for Halji glacier compared to the resolution of 30 m (see Figure 5). With the presented setup, the deviations of $B_{clim,a}$ to the ∼30 m simulation are up to ∼100 m resolution in a tolerable range (see Section 3.3).

5.1.2. COSIPY Simulation Uncertainties

COSIPY is a point model with no lateral exchange of energy and mass. In its distributed setup, at each GGP all processes are calculated without any exchange with neighboring grid cells. Furthermore, over a period of 40 years, ice-dynamics play an important role. Nevertheless, due to its very low flow velocities (see Appendix A Figure A1), mass balance response of the Halji glacier can be analyzed concerning meteorological forcing only. An approximated mean flow velocity of 2.3 m a^{-1} ([47], dataset: [48]) would result in 90 m ice movement over the whole period of 40 years. However, for further long-term integration of glacier change ice-dynamics will have to be integrated into the modeling framework. Snowdrift and direct sublimation of falling snow are further processes that are not resolved by the model. The model has been among others applied to the Zhadang glacier (see Section 5.1 in Sauter et al. [42]) and the Urumqi Glacier No. 1 (see Thiel et al. [95]), both located in HMA. The simulations in both cases revealed reasonable results. To assess the uncertainties stemming from all parameters and constants a full Monte Carlo simulation would have to be executed for the Halji glacier, which is not feasible in this study due to the enormous computational demand. A statistical error would affect single years, but not a long term cumulative value because the error would decrease according to the central limit theorem [96]. A systematic error would indeed affect the cumulative value of B_{clim}. Due to the significant correlation between α and $B_{clim,a}$ and experiences from Mölg et al. [58], Sauter et al. [42] and Thiel et al. [95], the Oerlemans and Knap [57] α parametrization is crucial for model output. We used the parameters of Mölg et al. [58]. For a sensitivity test, we varied the α values for fresh snow, firn and ice within the uncertainties of their study. The fresh snow α variance results in ±0.5 m w.e. a^{-1} feedback, the firn variance in a ±0.43 m w.e. a^{-1} feedback and the ice variance in a ±0.17 m w.e. a^{-1} feedback. The test shows the high sensitivity to the albedo parametrization. Therefore, COSIPY simulated b_{clim} always has to be evaluated against remote-sensing based geodetic mass balance or mass balance derived from the glaciological method through direct observations on the ground. If B_{clim} lies within a reasonable range compared to the independent evaluation data, we understand the main purpose of applying COSIPY in identifying drivers of seasonal and interannual mass balance variability and in advancing process understanding of interactions between atmospheric drivers and B_{clim}. These analyses are feasible and justified when overall calculated B_{clim} falls within a reasonable range. This has also been demonstrated in other studies using medium complexity energy and mass balance models similar to COSIPY (e.g., [97–102]).

5.2. Glacier-Wide Climatic Mass Balance

Mean simulated $B_{clim,a}$ of the MB-years 1982 to 2019 is −0.48 m w.e. a^{-1}. Model simulations can be compared to ice volume changes derived by remote sensing studies of Kropáček et al. [38] and Shean et al. [7] on the mass budget of the Halji glacier. Those values are summarized in Table 6. Corresponding simulated $B_{clim,a}$ falls within the range of uncertainty in the case of the study by Kropáček et al. [38]. In the case of Shean et al. [7], the COSIPY simulated result is less negative than their estimate. Overall, the simulated negative B_{clim} falls within a reasonable range and is in line with observed reduction in area, presented by the various outlines in Figure 1, the general glacier retreat in HMA (e.g., [3–6]) and in particular in western Nepal (e.g., [19,103,104]). A possible explanation for the more negative result of the Shean et al. [7] study are the simulated extreme negative MB-years 2016, 2017 and 2018. which are included in their study period, while they are not included in the Kropáček et al. [38] study.

Table 6. Comparison of simulated annual glacier-wide climatic mass balance $B_{clim,a}$ (m w.e. a^{-1}) with other studies using digital elevation model differences at the Halji glacier.

Mass-Balance Year	COSIPY	Kropáček et al. [38]	Shean et al. ([7], Dataset: [49])
1982–2019	−0.48	-	-
2001–2013	−0.35	-0.40 ± 0.30	-
2001–2018	−0.53	-	-0.70 ± 0.15

COSIPY simulations show a high interannual variability of $B_{clim,a}$ with a standard deviation of 0.71 m w.e. a^{-1}. The simulated mass budget between 2001 and 2010 is clearly negative. Nevertheless, this finding is not that obvious in the changes of glacier outlines between 2001 and 2010. Possibly, in this period, the negative mass balance was mainly a result of glacier thinning as opposed to area reduction. With the currently available dataset, we cannot evaluate this possibility in more detail.

Concerning the COSIPY forcing variables, the variability of B_{clim} is mostly determined by T_2 and TP. The high correlation of B_{clim} with U_2 and RH_2 can be explained with their co-correlations with T_2. The clear shift in the pattern of monthly means of Q_{SWin} between October and April for the two periods before and after 2005/2006 seems to have no distinct influence on monthly deviations of B_{clim}. Especially, because the shift from 2005 on would be negative for the glacier budget whereas B_{clim} is most positive between 2008 and 2015. The intermediate variable SF_c is a result of the available amount of TP and T_2. The latter separates TP in liquid and solid precipitation and determines together with U_2 the density of fresh snow within COSIPY. A high correlation ($r_s = 0.54$, p-value < 0.01) is found between the annual variability of SF_c and $B_{clim,a}$. The combination of SF_c and surface melt patterns determines the variability of α, which has the highest correlation with $B_{clim,a}$ with $r_s = 0.8$ (p-value < 0.01) on annual bases. August is the second last month in the MB-year but still $B_{clim,a}$ is extremely sensitive to α variability in August with $r_s = 0.91$ (p-value < 0.01). Monthly deviations to their long-term mean of α in June, July and August reveal their strong coupling to monthly B_{clim} variability in the same months. July, August and September are the months with the highest monthly variability of B_{clim} in comparison with their long-term mean. Although monthly T_2 variability in the same months is smallest compared to the rest of the year this variability is nonetheless of major importance. These results are backed by the SSC, which reveal that peak in T_2 and TP sensitivity occurs during summer. In comparison with the SSC of the six glaciers from different mountain ranges in the world and including only Abramov glacier from HMA presented in Oerlemans and Reichert [43], Halji glacier is the only one with this behavior. Moreover, the difference between the sensitivity to December and November compared to September, August, and July is greater than for any glacier studied by Oerlemans and Reichert [43]. However, the applied mass balance model is not the same and differences resulting solely from the sensitivities of the applied models cannot be evaluated.

When looking at monthly mean deviations to their long-term mean in Figure 7, a possible explanation of the equilibrium state between 2008 and 2015 might be an increased TP amount, and therefore increased SF_c between June and September, resulting in a positive albedo feedback (see [28]). This feedback can partly be linked to the high correlation of the WYM and $B_{clim,a}$. The annual value of the WYM is ten years in a row negative between 2005 and 2015. In contrast, there are only three consecutive negative years of the WYM from 1984 to 2004. The WYM is a measure for the large-scale monsoon circulation intensity [79,105]. Besides the high correlations between WYM and $B_{clim,a}$, a high correlation with $r_s = -0.45$ (p-value < 0.01) between June values of WYM and α highlights again the importance of α.

The correlations between B_{clim} and WYM and B_{clim} and the forcing variables emphasize the importance of timing and strength of the monsoon for the Halji glacier. The correlations among the forcing variables T_2, RH_2, U_2 and Q_{LWin} in June are further indications of the importance of the monsoon. A strong monsoon with an unstable atmosphere is accompanied by higher T_2, higher U_2, higher Q_{LWin} and decreased RH_2. Remarkably,

other than the WYM, none of the other monsoon (e.g., Indian Summer Monsoon index, Australian Monsoon Index) or monsoon related (e.g., Indian Ocean Dipol index, Southern Oscillation Index) indices revealed a significant correlation within this study. The analysis of possible reasons is beyond the scope of this study and would be speculative at this point.

A couple of studies have shown the connection between POL and precipitation patterns (e.g., [82,106,107]), whereby they focus on the central and whole Tibetan Plateau, North China or winter precipitation patterns in the Karakoram or western Himalaya. In contrast, in case of Halji glacier, the high correlation of POL in June and $B_{clim,a}$ might rather be related to T_2 than to TP with $r_s = -0.47$ (p-value < 0.01) between June values of T_2 and POL.

All results of this study reveal that a high amount of Halji glaciers interannual $B_{clim,a}$ variability can be accounted to the variability of T_2 and TP in summer, which can be at least partly be due to monsoon patterns. This finding is in accordance with the literature (e.g., [19,108]). As a result, Halji glacier is extremely sensitive to temperatures changes. An increase in T_2 of 0.5 K results in a $B_{clim,a}$ of −1.23 m w.e. a^{-1} (−0.75 m w.e. a^{-1} difference compared to reference simulation), which mainly affects B_{clim} during summer. An increase in summer temperature has three main negative effects on the glacier mass budget for that kind of glacier [25]: (1) Enhanced melt, (2) lowered ratio between solid and liquid precipitation, which results in less surface accumulation, and (3) lower values of α as a result of a decrease in SF_c, which enlarges Q_{SWnet} and results in further enhancement of melt. The latter two effects are denoted as the snow-albedo feedback [26–28].

6. Conclusions

We simulated a $B_{clim,a}$ of −0.48 m w.e. a^{-1} between October 1981 and September 2019 for the Halji glacier in northwestern Nepal. Given the lack of direct mass balance observations, simulations were compared to geodetic mass balances derived from two remote sensing studies [7,38]. The simulation results are in a reasonable range compared to both of these remote sensing studies. The simulation also reveals high interannual variability of $B_{clim,a}$. All results revealed the importance of the monsoon and T_2 and TP in summer for the variability of $B_{clim,a}$. Only the combination of effects and resulting variability of α can explain the pronounced B_{clim} variability in this season. The peak in summer of the calculated seasonal sensitivity characteristic back these findings. The variability of forcing variables in winter has a minor influence on $B_{clim,a}$.

Comparison of ERA5-L derived COSIPY forcing variables with AWS measured variables revealed that most input data related uncertainties arise from the amount of TP and that downscaling and scaling procedures are necessary in order to obtain reliable model forcing data. A decrease of 20 % in TP results in an annual glacier-wide climatic mass balance of −1.77 m w.e. a^{-1}. Therefore, there is an urgent need in spatially higher resolved atmospheric datasets, to serve as forcing for long-term runs of mass balance models.

Presented approaches and statistics revealed that downscaling of T_2, p_{sfc} and RH_2 is straight-forward given that some observations in the field are available. Furthermore, we recommend to investigate the influence of the applied spatial resolution on B_{clim} for each study site individually in order to identify the best trade-off between computational power and reasonable results.

COSIPY proves to be a powerful tool to identify climatic drivers of seasonal and interannual mass balance variability and to improve the process understanding of glacier responses to atmospheric forcing.

Author Contributions: Conceptualization, A.A. and C.S.; methodology, A.A. and C.S.; software, A.A.; validation, A.A., D.S. and C.S.; formal analysis, A.A.; investigation, A.A.; resources, D.S.; data curation, A.A. and D.S.; writing—original draft preparation, A.A.; writing—review and editing, C.S. and D.S.; visualization, A.A.; supervision, C.S.; project administration, A.A., D.S. and C.S.; funding acquisition, C.S. and D.S. All authors have read and agreed to the published version of the manuscript.

Funding: This research was funded by the German Research Foundation's (DFG) research grants 'Precipitation patterns, snow and glacier response in High Asia and their variability on sub-decadal time scales, sub-project: snow cover and glacier energy and mass balance variability' (prime-SG, SCHN 680/13-1), 'Dynamic Response of Glaciers in the Qilian Shan to Climate Change' (Dyn-Q, SCHN 680/17-1), and 'Glacial lake outburst floods in the Halji region, Nepal' (Halji, SCHN 680/19-1 and SCHE 750/17-1).

Data Availability Statement: The data presented in this study are available on request from the corresponding author.

Acknowledgments: We are grateful to Benjamin Schröter for organizing and supporting the field trips to Halji glacier. Further, we thank Tom Grassmann, Manfred Buchroithner, Nico Rohrbach and the community of Halji for their support of and contribution to field work. We would also like to thank the two anonymous reviewers and the editors, who substantially helped to improve the study. We acknowledge support by the German Research Foundation (DFG) and the Open Access Publication Fund of Humboldt-Universität zu Berlin.

Conflicts of Interest: The authors declare no conflict of interest. The funders had no role in the design of the study, in the collection, analyses, or interpretation of data, in the writing of the manuscript, or in the decision to publish the results.

Abbreviations

The following acronyms are used in this manuscript:

AMI	Australian Monsoon Index
AMO	Atlantic Multi-decadal Oscillation
AO	Arctic Oscillation index
AWS	automatic weather station
COSIPY	COupled Snowpack and Ice surface energy and mass balance model in PYthon
DEM	digital elevation model
EA	East Atlantic index
EATL/WRUS	East Atlantic/ West Russia index
ECMWF	European Centre for Medium-Range Weather Forecasts
ERA5	ECMWF Reanalysis fifth generation
ERA5-L	ECMWF Reanalysis fifth generation-Land
GDAL	Geospatial Data Abstraction Library
GGP	glacier grid point
GLOF	glacial lake outburst flood
H-TESSEL	Hydrology revised Tiled ECMWF Scheme for Surface Exchanges over Land
HMA	High Mountain Asia
HPCC	High-Performance Computing Cluster
IOD	Indian Ocean Dipol index
ISM	Indian Summer Monsoon index
MB	mass balance
MB-year	mass-balance year
MBE	mean bias error
MEI	Multivariate ENSO Index
NAO	North Atlantic Oscillation
Nino1+2	Nino 1+2 index
Nino34	Nino 3.4 index
Nino4	Nino 4 index
ONI	Oceanic Nino Index
PDO	Pacific Decadal Oscillation
PNA	Pacific/North American index
POL	Polar/Eurasia index
RGI6	Randolph Glacier Inventory 6.0
RMSE	root mean square error
SCAND	Scandinavia index
SEB	surface energy balance
SOI	Southern Oscillation Index
SRTM	Shuttle Radar Topography Mission
SSC	seasonal sensitivity characteristic
TNI	Trans-Niño Index
WNPM	Western North Pacific Monsoon index
WP	West Pacific index
WYM	Webster and Yang Monsoon index

The following constants are used in this manuscript:

Symbol	Description	Unit	Default Value
M	average molar mass of air	kg mol^{-1}	0.02897
R	gas constant	kg m^2 (s^2 mol K)$^{-1}$	8.314462
T_m	melting point temperature	K	273.16
g	gravitational acceleration	m s^{-2}	9.80665

The following symbols are used in this manuscript:

Symbol	Description	Unit
$B_{clim,a}$	annual glacier-wide climatic mass balance	m w.e.
$B_{clim,cum}$	glacier-wide cumulative climatic mass balance	m w.e.
B_{clim}	glacier-wide climatic mass balance	m w.e.
Q_E	latent heat flux	W m^{-2}
Q_G	glacier heat flux	W m^{-2}
Q_H	sensible heat flux	W m^{-2}
Q_M	available melt energy	W m^{-2}
Q_R	sensible heat flux of rain	W m^{-2}
Q_{LWin}	incoming longwave radiation	W m^{-2}
Q_{LWnet}	net longwave radiation	W m^{-2}
Q_{LWout}	outgoing longwave radiation	W m^{-2}
Q_{SWin}	incoming shortwave radiation	W m^{-2}
Q_{SWnet}	net shortwave radiation	W m^{-2}
RH_2	relative humidity at 2 m	%
SF_c	accumulated snowfall	m w.e.
SH_2	specific humidity at 2 m	g kg^{-1}
TP	total precipitation	mm
T_0	air temperature at reference height	K
T_l	layer temperature	K
T_s	surface temperature	K
T_2	air temperature at 2 m	K
$T_{d,2}$	dewpoint temperature at 2 m	K
U_2	wind speed at 2 m	m s^{-1}
U_{10}	wind speed at 10 m	m s^{-1}
α	snow/ice albedo	-
a_i	internal ablation	m w.e.
a_{sfc}	surface ablation	m w.e.
a	thermal gradient	K m^{-1}
$b_{clim,a}$	annual climatic mass balance	m w.e.
$b_{clim,cum}$	cumulative climatic mass balance	m w.e.
b_{clim}	climatic mass balance	m w.e.
b_i	internal mass balance	m w.e.
b_{sfc}	surface mass balance	m w.e.
c_i	internal accumulation	m w.e.
c_{sfc}	surface accumulation	m w.e.
h	height difference	m
p_0	atmospheric pressure at reference height	hPa
p_{sfc}	surface pressure	hPa
p-value	p-value	-
r^2	coefficient of determination	-
r_s	Spearman's rank correlation coefficient	-
z_0	surface roughness	m

Appendix A

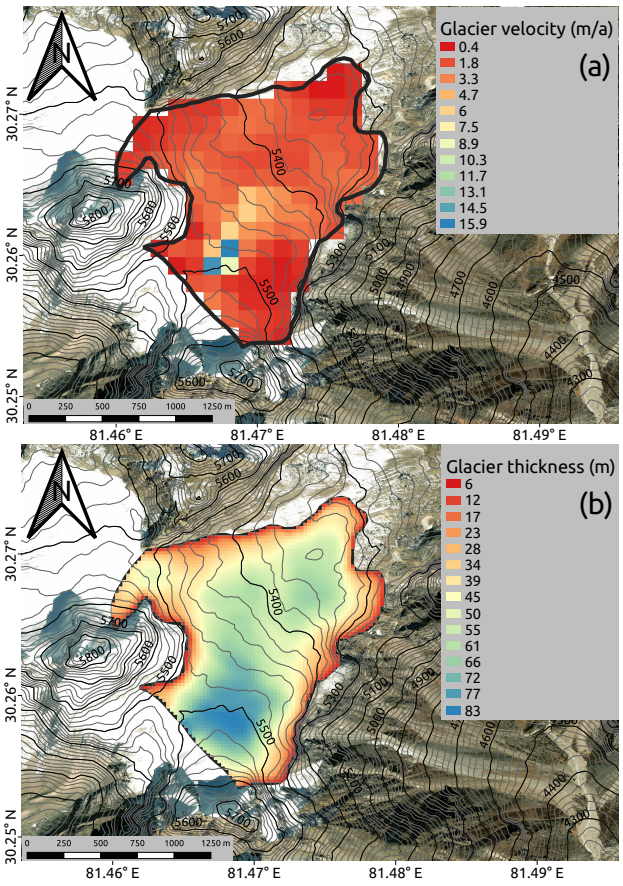

Figure A1. Glacier velocity (**a**) according to Dehecq et al. ([47], dataset: [48]]) and Glacier thickness (**b**) according to Farinotti et al. ([22], dataset: [46]]) of Halji glacier with a satellite image map in the background [55]. For the location of Halji glacier please refer to Figure 1.

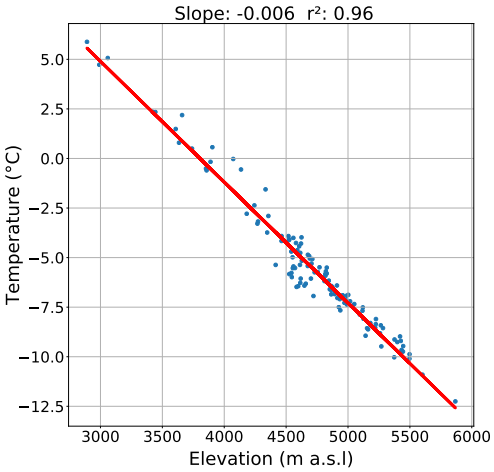

Figure A2. Scatterplot of ERA5-L air temperature at 2 m and model elevations of the 121 ERA5-L grid cells around the location of Halji glacier. The temperatures are the long-term means of each grid cell from 1981 to 2019.

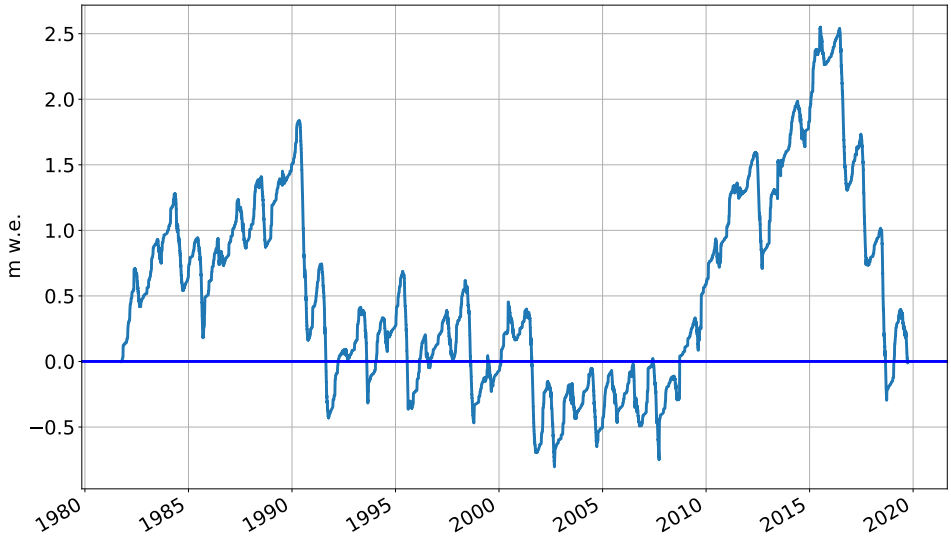

Figure A3. Cumulative climatic mass balance of temperature adjusted simulation of Halji glacier from 1981 to 2020. We apply a temperature offset of −0.37 K to reach the long-term zero cumulative climatic mass balance which is needed for the computation of the seasonal sensitivity characteristic according to Oerlemans and Reichert [43].

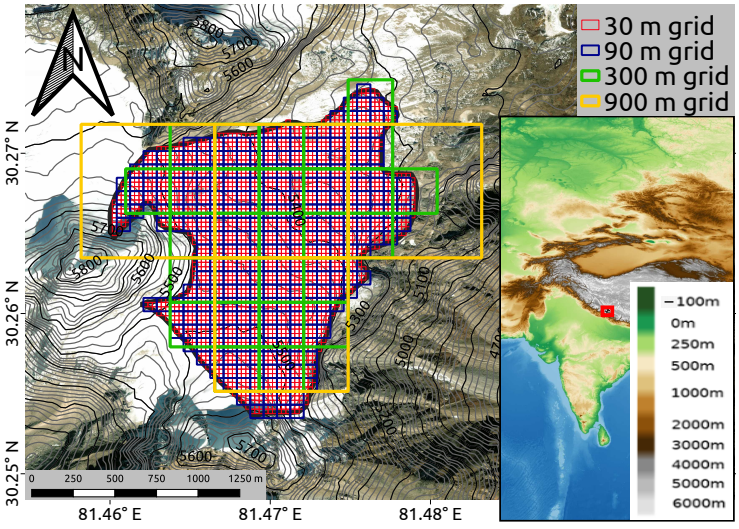

Figure A4. Differently resolved spatial grids over Halji glacier based on the glacier outline from Randolph Glacier Inventory 6.0 [45] and with a satellite image map as background from [55]. Colors within the inset map represent elevation [56].

Table A1. Investigated circulation, oscillation and monsoon indexes; The temporal resolution and coverage (status 1 August 2020) are displayed in the third column.

Index	Description	Temporal Resolution and Coverage
AMI [109]	Australian Monsoon Index	Seasonal (DJF), 1948–2014
http://apdrc.soest.hawaii.edu/projects/monsoon/seasonal-monidx.html, accessed on 22 March 2021		
AMO [110]	Atlantic Multi-decadal Oscillation	Annual, 1870–2010
https://climatedataguide.ucar.edu/climate-data/atlantic-multi-decadal-oscillation-amo, accessed on 22 March 2021		
AO [111]	Arctic Oscillation index	Monthly, January 1950–April 2020
https://www.cpc.ncep.noaa.gov/products/precip/CWlink/daily_ao_index/ao.shtml, accessed on 22 March 2021		
EA [80]	East Atlantic index	Monthly, January 1950–April 2020
https://www.cpc.ncep.noaa.gov/data/teledoc/ea.shtml, accessed on 22 March 2021		
EATL/WRUS [80]	East Atlantic/ West Russia index	Monthly, January 1950–April 2020
https://www.cpc.ncep.noaa.gov/data/teledoc/eawruss.shtml, accessed on 22 March 2021		
IOD [112]	Indian Ocean Dipol index	Monthly, January 1870–December 2018
http://www.bom.gov.au/climate/enso/indices/about.shtml, accessed on 22 March 2021		
ISM [113,114]	Indian Summer Monsoon index	Seasonal (JJAS), 1948–2015
http://apdrc.soest.hawaii.edu/projects/monsoon/seasonal-monidx.html, accessed on 22 March 2021		
MEI [115]	Multivariate ENSO Index	Monthly, January 1979–December 2019
https://psl.noaa.gov/enso/mei/, accessed on 22 March 2021		
NAO [116]	North Atlantic Oscillation	Monthly, January 1899–February 2020
https://climatedataguide.ucar.edu/climate-data/hurrell-north-atlantic-oscillation-nao-index-pc-based, accessed on 22 March 2021		
Nino1+2 [117]	Nino 1+2 index	Monthly, January 1950–June 2020
https://climatedataguide.ucar.edu/climate-data/nino-sst-indices-nino-12-3-34-4-oni-and-tni, accessed on 22 March 2021		
Nino34 [117]	Nino 3.4 index	Monthly, January 1950–June 2020
https://climatedataguide.ucar.edu/climate-data/nino-sst-indices-nino-12-3-34-4-oni-and-tni, accessed on 22 March 2021		
Nino4 [117]	Nino 4 index	Monthly, January 1950–June 2020
https://climatedataguide.ucar.edu/climate-data/nino-sst-indices-nino-12-3-34-4-oni-and-tni, accessed on 22 March 2021		
ONI [117]	Oceanic Nino Index	Monthly, January 1950–May 2020
https://climatedataguide.ucar.edu/climate-data/nino-sst-indices-nino-12-3-34-4-oni-and-tni, accessed on 22 March 2021		
PDO [118]	Pacific Decadal Oscillation	Monthly, January 1854–February 2020
https://www.ncdc.noaa.gov/teleconnections/pdo/, accessed on 22 March 2021		
PNA [119]	Pacific/North American index	Monthly, January 1950–April 2020
https://www.cpc.ncep.noaa.gov/data/teledoc/pna.shtml, accessed on 22 March 2021		
POL [80]	Polar/Eurasia index	Monthly, January 1950–April 2020
https://www.cpc.ncep.noaa.gov/data/teledoc/poleur.shtml, accessed on 22 March 2021		
SCAND [80]	Scandinavia index	Monthly, January 1950–June 2020
https://www.cpc.ncep.noaa.gov/data/teledoc/scand.shtml, accessed on 22 March 2021		
SOI [120]	Southern Oscillation Index	Monthly, January 1951–December 2019
https://www.ncdc.noaa.gov/teleconnections/enso/indicators/soi/, accessed on 22 March 2021		
TNI [117]	Trans-Niño Index	Monthly, January 1948–April 2020
https://climatedataguide.ucar.edu/climate-data/nino-sst-indices-nino-12-3-34-4-oni-and-tni, accessed on 22 March 2021		
WNPM [113,114]	Western North Pacific Monsoon index	Seasonal (JJAS), 1948–2015
http://apdrc.soest.hawaii.edu/projects/monsoon/seasonal-monidx.html, accessed on 22 March 2021		
WP [80,119]	West Pacific index	Monthly, January 1950–April 2020
https://www.cpc.ncep.noaa.gov/data/teledoc/wp.shtml, accessed on 22 March 2021		
WYM [40]	Webster and Yang Monsoon index	Seasonal (JJAS), 1948–2015
http://apdrc.soest.hawaii.edu/projects/monsoon/seasonal-monidx.html, accessed on 22 March 2021		

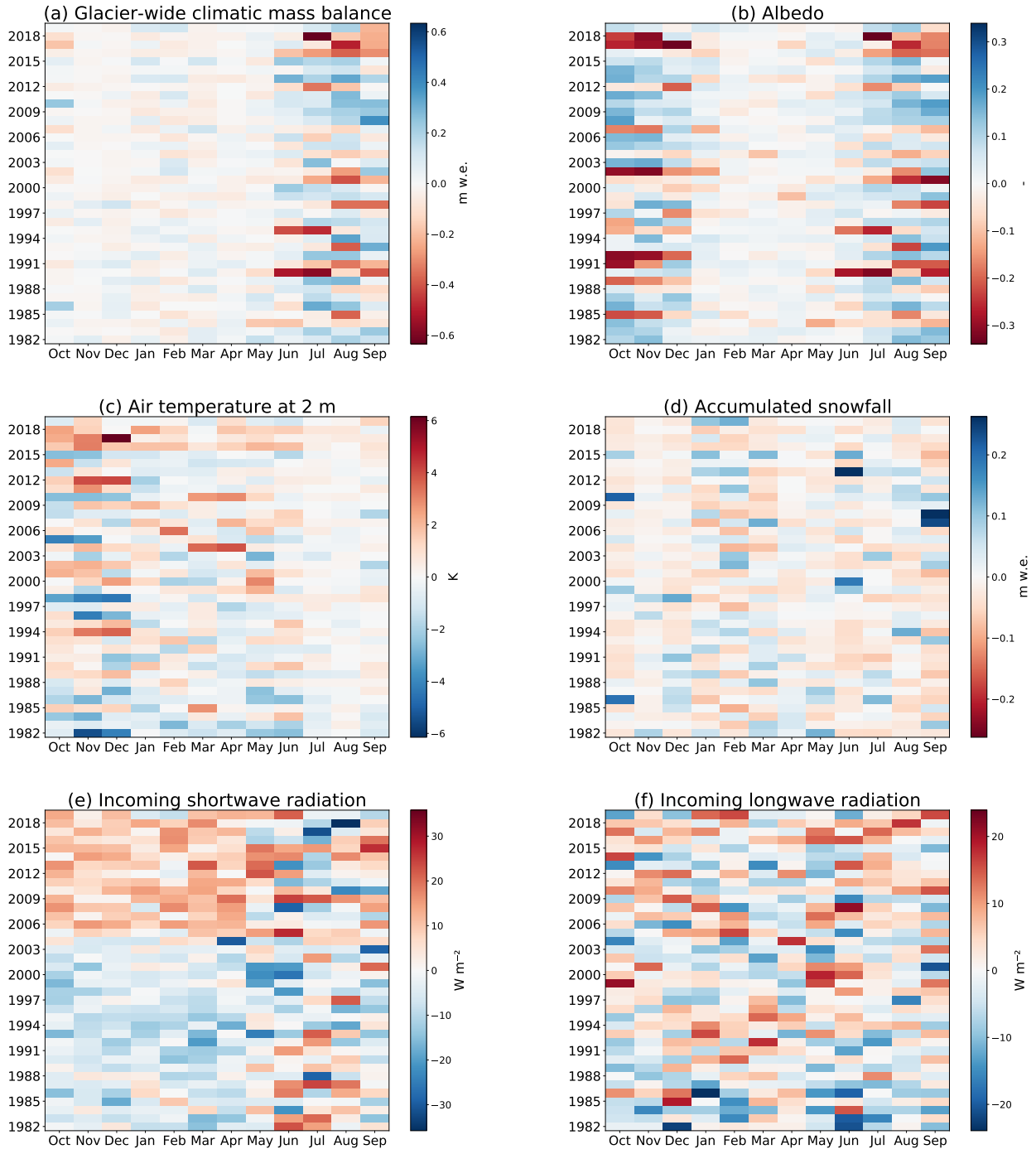

Figure A5. Monthly mean deviations 1982 to 2019 from long-term monthly mean values of glacier-wide climatic mass balance (**a**), albedo (**b**), air temperature at 2 m (**c**), accumulated snowfall (**d**), incoming shortwave radiation (**e**) and incoming longwave radiation (**f**). The color bar is arranged so that deviations that act positively (negatively) on glacier-wide climatic mass balance are shown in blue (red).

References

1. Bolch, T.; Pieczonka, T.; Benn, D.I. Multi-decadal mass loss of glaciers in the Everest area (Nepal Himalaya) derived from stereo imagery. *Cryosphere* **2011**, *5*, 349–358. [CrossRef]
2. Lei, Y.; Yao, T.; Yi, C.; Wang, W.; Sheng, Y.; Li, J.; Joswiak, D. Glacier mass loss induced the rapid growth of Linggo Co on the central Tibetan Plateau. *J. Glaciol.* **2012**, *58*, 177–184. [CrossRef]
3. Neckel, N.; Kropáček, J.; Bolch, T.; Hochschild, V. Glacier mass changes on the Tibetan Plateau 2003–2009 derived from ICESat laser altimetry measurements. *Environ. Res. Lett.* **2014**, *9*, 014009. [CrossRef]
4. Kang, S.; Wang, F.; Morgenstern, U.; Zhang, Y.; Grigholm, B.; Kaspari, S.; Schwikowski, M.; Ren, J.; Yao, T.; Qin, D.; Mayewski, P.A. Dramatic loss of glacier accumulation area on the Tibetan Plateau revealed by ice core tritium and mercury records. *Cryosphere* **2015**, *9*, 1213–1222. [CrossRef]
5. Liu, L.; Jiang, L.; Jiang, H.; Wang, H.; Ma, N.; Xu, H. Accelerated glacier mass loss (2011–2016) over the Puruogangri ice field in the inner Tibetan Plateau revealed by bistatic InSAR measurements. *Remote Sens. Environ.* **2019**, *231*, 111241. [CrossRef]
6. Liu, L.; Jiang, L.; Zhang, Z.; Wang, H.; Ding, X. Recent Accelerating Glacier Mass Loss of the Geladandong Mountain, Inner Tibetan Plateau, Estimated from ZiYuan-3 and TanDEM-X Measurements. *Remote Sens.* **2020**, *12*, 472. [CrossRef]
7. Shean, D.E.; Bhushan, S.; Montesano, P.; Rounce, D.R.; Arendt, A.; Osmanoglu, B. A Systematic, Regional Assessment of High Mountain Asia Glacier Mass Balance. *Front. Earth Sci.* **2020**, *7*, 363. [CrossRef]
8. Rounce, D.R. Glacier Mass Change in High Mountain Asia Through 2100 Using the Open-Source Python Glacier Evolution Model (PyGEM). *Front. Earth Sci.* **2020**, *7*, 20. [CrossRef]
9. Wang, S.; Zhang, M.; Wang, B.; Sun, M.; Li, X. Recent changes in daily extremes of temperature and precipitation over the western Tibetan Plateau, 1973–2011. *Quat. Int.* **2013**, *313–314*, 110–117. [CrossRef]
10. Wei, Y.; Fang, Y. Spatio-Temporal Characteristics of Global Warming in the Tibetan Plateau during the Last 50 Years Based on a Generalised Temperature Zone—Elevation Model. *PLoS ONE* **2013**, *8*, e60044. [CrossRef] [PubMed]
11. Schiemann, R.; Lüthi, D.; Schär, C. Seasonality and interannual variability of the westerly jet in the Tibetan Plateau region. *J. Clim.* **2009**, *22*, 2940–2957. [CrossRef]
12. Mölg, T.; Maussion, F.; Scherer, D. Mid-latitude westerlies as a driver of glacier variability in monsoonal High Asia. *Nat. Clim. Chang.* **2013**, *4*, 68–73. [CrossRef]
13. Xu, X.; Zhao, T.; Lu, C.; Guo, Y.; Chen, B.; Liu, R.; Li, Y.; Shi, X. An important mechanism sustaining the atmospheric "water tower" over the Tibetan Plateau. *Atmos. Chem. Phys.* **2014**, *14*, 11287–11295. [CrossRef]
14. Curio, J.; Maussion, F.; Scherer, D. A 12-year high-resolution climatology of atmospheric water transport over the Tibetan Plateau. *Earth Syst. Dyn.* **2015**, *6*, 109–124. [CrossRef]
15. Curio, J.; Scherer, D. Seasonality and spatial variability of dynamic precipitation controls on the Tibetan Plateau. *Earth Syst. Dyn.* **2016**, *7*, 767–782. [CrossRef]
16. Ma, Y.; Lu, M.; Chen, H.; Pan, M.; Hong, Y. Atmospheric moisture transport versus precipitation across the Tibetan Plateau: A mini-review and current challenges. *Atmos. Res.* **2018**, *209*, 50–58. [CrossRef]
17. Li, S.; Yao, T.; Yang, W.; Yu, W.; Zhu, M. Glacier Energy and Mass Balance in the Inland Tibetan Plateau: Seasonal and Interannual Variability in Relation to Atmospheric Changes. *J. Geophys. Res. Atmos.* **2018**, *123*, 6390–6409. [CrossRef]
18. Wang, X.; Pang, G.; Yang, M. Precipitation over the Tibetan Plateau during recent decades: A review based on observations and simulations: PRECIPITATION ON THE TIBETAN PLATEAU. *Int. J. Climatol.* **2018**, *38*, 1116–1131. [CrossRef]
19. Yao, T.; Thompson, L.; Yang, W.; Yu, W.; Gao, Y.; Guo, X.; Yang, X.; Duan, K.; Zhao, H.; Xu, B.; et al. Different glacier status with atmospheric circulations in Tibetan Plateau and surroundings. *Nat. Clim. Chang.* **2012**, *2*, 663–667. [CrossRef]
20. Gardelle, J.; Berthier, E.; Arnaud, Y.; Kääb, A. Region-wide glacier mass balances over the Pamir-Karakoram-Himalaya during 1999–2011. *Cryosphere* **2013**, *7*, 1263–1286. [CrossRef]
21. Bonekamp, P.N.J.; de Kok, R.J.; Collier, E.; Immerzeel, W.W. Contrasting Meteorological Drivers of the Glacier Mass Balance Between the Karakoram and Central Himalaya. *Front. Earth Sci.* **2019**, *7*, 107. [CrossRef]
22. Farinotti, D.; Huss, M.; Fürst, J.J.; Landmann, J.; Machguth, H.; Maussion, F.; Pandit, A. A consensus estimate for the ice thickness distribution of all glaciers on Earth. *Nat. Geosci.* **2019**, *12*, 168–173. [CrossRef]
23. Ageta, Y.; Higuchi, K. Estimation of Mass Balance Components of a Summer-Accumulation Type Glacier in the Nepal Himalaya. *Geogr. Annaler. Ser. A, Phys. Geogr.* **1984**, *66*, 249. [CrossRef]
24. Maussion, F.; Scherer, D.; Mölg, T.; Collier, E.; Curio, J.; Finkelnburg, R. Precipitation Seasonality and Variability over the Tibetan Plateau as Resolved by the High Asia Reanalysis*. *J. Clim.* **2014**, *27*, 1910–1927. [CrossRef]
25. Naito, N. Summer Accumulation Type Glaciers. In *Encyclopedia of Snow, Ice and Glaciers*; Singh, V.P., Singh, P., Haritashya, U.K., Eds.; Encyclopedia of Earth Sciences Series; Springer: Dordrecht, The Netherlands, 2011; pp. 1107–1108. [CrossRef]
26. Qu, X.; Hall, A. What Controls the Strength of Snow-Albedo Feedback? *J. Clim.* **2007**, *20*, 3971–3981. [CrossRef]
27. Qu, X.; Hall, A. On the persistent spread in snow-albedo feedback. *Clim. Dyn.* **2014**, *42*, 69–81. [CrossRef]
28. Ghatak, D.; Sinsky, E.; Miller, J. Role of snow-albedo feedback in higher elevation warming over the Himalayas, Tibetan Plateau and Central Asia. *Environ. Res. Lett.* **2014**, *9*, 114008. [CrossRef]
29. Wang, X.; Siegert, F.; Zhou, A.G.; Franke, J. Glacier and glacial lake changes and their relationship in the context of climate change, Central Tibetan Plateau 1972–2010. *Glob. Planet. Chang.* **2013**, *111*, 246–257. [CrossRef]

30. Treichler, D.; Kääb, A.; Salzmann, N.; Xu, C.Y. Recent glacier and lake changes in High Mountain Asia and their relation to precipitation changes. *Cryosphere* **2019**, *13*, 2977–3005. [CrossRef]
31. Haeberli, W. Frequency and Characteristics of Glacier Floods in the Swiss Alps. *Ann. Glaciol.* **1983**, *4*, 85–90. [CrossRef]
32. Björnsson, H. Jökulhlaups in Iceland: Prediction, characteristics and simulation. *Ann. Glaciol.* **1992**, *16*, 95–106. [CrossRef]
33. Huggel, C.; Kääb, A.; Haeberli, W.; Teysseire, P.; Paul, F. Remote sensing based assessment of hazards from glacier lake outbursts: A case study in the Swiss Alps. *Can. Geotech. J.* **2002**, *39*, 316–330. [CrossRef]
34. Veh, G.; Korup, O.; von Specht, S.; Roessner, S.; Walz, A. Unchanged frequency of moraine-dammed glacial lake outburst floods in the Himalaya. *Nat. Clim. Chang.* **2019**, *9*, 379–383. [CrossRef]
35. Wester, P.; Mishra, A.; Mukherji, A.; Shrestha, A.B., Eds. *The Hindu Kush Himalaya Assessment: Mountains, Climate Change, Sustainability and People*; Springer International Publishing: Cham, Switzerland, 2019. [CrossRef]
36. Hovden, A. Who were the sponsors? Reflections on recruitment and ritual economy in three Himalayan village monasteries. In *Tibetans Who Escaped the Historians Net: Studies in the Social History of Tibetan Societies*; Ram ble, C., Schwieger, P., Travers, A., Eds.; Vajra Publications: Kathmandu, Nepal, 2013; pp. 209–230.
37. Diemberger, H.; Hovden, A.; Yeh, E.T. The honour of the snow-mountains is the snow: Tibetan livelihoods in a changing climate. In *The High-Mountain Cryosphere: Environmelt Changes and Human Risks*; Huggel, C., Carey, M., Clague, J.J., Kaab, A., Eds.; Cambridge University Press: Cambridge, UK, 2015; pp. 249–271. [CrossRef]
38. Kropáček, J.; Neckel, N.; Tyrna, B.; Holzer, N.; Hovden, A.; Gourmelen, N.; Schneider, C.; Buchroithner, M.; Hochschild, V. Repeated glacial lake outburst flood threatening the oldest Buddhist monastery in north-western Nepal. *Nat. Hazards Earth Syst. Sci.* **2015**, *15*, 2425–2437. [CrossRef]
39. Benn, D.I.; Owen, L.A. The role of the Indian summer monsoon and the mid-latitude westerlies in Himalayan glaciation: Review and speculative discussion. *J. Geol. Soc.* **1998**, *155*, 353–363. [CrossRef]
40. Webster, P.J.; Magaña, V.O.; Palmer, T.N.; Shukla, J.; Tomas, R.A.; Yanai, M.; Yasunari, T. Monsoons: Processes, predictability, and the prospects for prediction. *J. Geophys. Res. Ocean.* **1998**, *103*, 14451–14510. [CrossRef]
41. Copernicus. Climate Data Store ERA5-Land Reanalysis. 2019. Available online: https://cds.climate.copernicus.eu/cdsapp#!/home (accessed on 11 Janaury 2021).
42. Sauter, T.; Arndt, A.; Schneider, C. COSIPY v1.3—An open-source coupled snowpack and ice surface energy and mass balance model. *Geosci. Model Dev.* **2020**, *13*, 5645–5662. [CrossRef]
43. Oerlemans, J.; Reichert, B. Relating glacier mass balance to meteorological data by using a seasonal sensitivity characteristic. *J. Glaciol.* **2000**, *46*, 1–6. [CrossRef]
44. Earth Resources Observation And Science (EROS) Center. *Shuttle Radar Topography Mission (SRTM) 1 Arc-Second Global*; U.S. Geological Survey: Reston, VA, USA, 2017.
45. Consortium, R.G.I. *Randolph Glacier Inventory 6.0*; NSIDC: Boulder, CO, USA, 2017; [CrossRef]
46. Farinotti, D. A consensus estimate for the ice thickness distribution of all glaciers on Earth—Dataset. In *Medium: Txt/Plain, Application/Zip, Image/Tiff, 12.48 GB*; ETH: Zurich, Switzerland, 2019. [CrossRef]
47. Dehecq, A.; Gourmelen, N.; Trouve, E. Deriving large-scale glacier velocities from a complete satellite archive: Application to the Pamir–Karakoram–Himalaya. *Remote Sens. Environ.* **2015**, *162*, 55–66. [CrossRef]
48. Dehecq, A.; Gourmelen, N.; Trouvé, E. *High Mountain Asia Glacier Velocities 2013–2015 (Landsat 8)*; Zenodo: Geneva, Switzerland, 2019. [CrossRef]
49. Shean, D.; Bhushan, S. *Zenodo, Geneva, Switzerland. Type: Dataset*. 2020. doi:10.5281/ZENODO.3600623. Available online: https://zenodo.org/record/3600624#.YF1M_twRXIU (accessed on 22 March 2021). [CrossRef]
50. Ye, Q.; Yao, T.; Kang, S.; Chen, F.; Wang, J. Glacier variations in the Naimona'nyi region, western Himalaya, in the last three decades. *Ann. Glaciol.* **2006**, *43*, 385–389. [CrossRef]
51. Racoviteanu, A.S.; Bajracharya, S.A. *GLIMS Glacier Database*; NSIDC: Boulder, CO, USA, 2008; [CrossRef]
52. Sakai, A.S.; Sakai, A.A. *GLIMS Glacier Database*; NSIDC: Boulder, CO, USA, 2018; [CrossRef]
53. Drusch, M.; Del Bello, U.; Carlier, S.; Colin, O.; Fernandez, V.; Gascon, F.; Hoersch, B.; Isola, C.; Laberinti, P.; Martimort, P.; et al. Sentinel-2: ESA's Optical High-Resolution Mission for GMES Operational Services. *Remote Sens. Environ.* **2012**, *120*, 25–36. [CrossRef]
54. Lea, J.M. The Google Earth Engine Digitisation Tool (GEEDiT) and the Margin change Quantification Tool (MaQiT) – simple tools for the rapid mapping and quantification of changing Earth surface margins. *Earth Surf. Dyn.* **2018**, *6*, 551–561. [CrossRef]
55. Microsoft. *Bing Maps*; Microsoft: Redmond, WA, USA, 2020.
56. Terrestris GmbH & Co. KG. TOPOGRAPHIC WMS. 2021. Available online: https://www.terrestris.de/de/topographic-wms/ (accessed on 11 Janaury 2021).
57. Oerlemans, J.; Knap, W.H. A 1 year record of global radiation and albedo in the ablation zone of Morteratschgletscher, Switzerland. *J. Glaciol.* **1998**, *44*, 231–238. [CrossRef]
58. Mölg, T.; Maussion, F.; Yang, W.; Scherer, D. The footprint of Asian monsoon dynamics in the mass and energy balance of a Tibetan glacier. *Cryosphere* **2012**, *6*, 1445–1461. [CrossRef]
59. Mazumder, S. *Numerical Methods for Partial Differential Equations: Finite Difference and Finite Volume Methods*; OCLC: ocn913556966; Academic Press: Amsterdam, The Netherlands, 2016.

60. Bintanja, R.; Van Den Broeke, M.R. The Surface Energy Balance of Antarctic Snow and Blue Ice. *J. Appl. Meteorol.* **1995**, *34*, 902–926. [CrossRef]
61. Anderson, E.A. *A Point Energy and Mass Balance Model of a Snow Cover*; Technical Report; National Weather Service (NWS): Silver Spring, MD, USA, 1976.
62. Boone, A. *Description du Schema de Neige ISBA-ES (Explicit Snow)*; Technical Report; Updated in November, 2009; Centre National de Recherches Météorologiques, Météo-France: Toulouse, France, 2004.
63. Cogley, J.G.; Hock, R.; A Rasmussen, L.; Arendt, A.; Bauder, A.; J Braithwaite, R.; Jansson, P.; Kaser, G.; Möller, M.; Nicholson, L.; et al. Glossary of glacier mass balance and related terms. *Int. Assoc. Cryospheric Sci.* **2011**. [CrossRef]
64. Kaser, G.; Fountain, A.; Jansson, P. *A Manual for Monitoring the Mass Balance of Mountain Glaciers*; IHP-VI, Technical Documents in Hydrology No. 59; UNESCO: Paris, France, 2003.
65. Neckel, N.; Kropáček, J.; Schröter, B.; Scherer, D. Effects of Cyclone Hudhud captured by a high altitude Automatic Weather Station in northwestern Nepal. *Weather* **2015**, *70*, 208–210. [CrossRef]
66. ECMWF. *ERA5-Land: Data Documentation*; ECMWF: Reading, UK, 2020.
67. Hersbach, H.; Bell, B.; Berrisford, P.; Hirahara, S.; Horányi, A.; Muñoz-Sabater, J.; Nicolas, J.; Peubey, C.; Radu, R.; Schepers, D.; et al. The ERA5 global reanalysis. *Q. J. R. Meteorol. Soc.* **2020**, qj.3803. [CrossRef]
68. Wohlfahrt, G.; Hammerle, A.; Niedrist, G.; Scholz, K.; Tomelleri, E.; Zhao, P. On the energy balance closure and net radiation in complex terrain. *Agric. For. Meteorol.* **2016**, *226–227*, 37–49. [CrossRef]
69. Lente, G.; Ősz, K. Barometric formulas: Various derivations and comparisons to environmentally relevant observations. *ChemTexts* **2020**, *6*, 13. [CrossRef]
70. Gudmundsson, L.; Bremnes, J.B.; Haugen, J.E.; Engen-Skaugen, T. Technical Note: Downscaling RCM precipitation to the station scale using statistical transformations—A comparison of methods. *Hydrol. Earth Syst. Sci.* **2012**, *16*, 3383–3390. [CrossRef]
71. ECMWF. IFS Documentation CY41R2—Part IV: Physical Processes. 2016. Available online: https://www.ecmwf.int/node/16648 (accessed on 9 December 2020).
72. ECMWF. *ERA5-Land: Data Documentation*; ECMWF: Reading, UK, 2021.
73. Stull, R.B. (Ed.) *An Introduction to Boundary Layer Meteorology*; Springer: Dordrecht, The Netherlands, 1988. [CrossRef]
74. Brock, B.W.; Willis, I.C.; Sharp, M.J. Measurement and parameterization of aerodynamic roughness length variations at Haut Glacier d'Arolla, Switzerland. *J. Glaciol.* **2006**, *52*, 281–297. [CrossRef]
75. Gromke, C.; Manes, C.; Walter, B.; Lehning, M.; Guala, M. Aerodynamic Roughness Length of Fresh Snow. *Bound.-Layer Meteorol.* **2011**, *141*, 21–34. [CrossRef]
76. GDAL/OGR Contributors. *GDAL/OGR Geospatial Data Abstraction Software Library*; Open Source Geospatial Foundation: Delaware, USA, 2020.
77. Zwillinger, D.; Kokoska, S. *CRC Standard Probability and Statistics Tables and Formulae*; Chapman & Hall/CRC: Boca Raton, FL, USA, 2000.
78. Reichert, B.K.; Bengtsson, L.; Oerlemans, J. Midlatitude Forcing Mechanisms for Glacier Mass Balance Investigated Using General Circulation Models. *J. Clim.* **2001**, *14*, 18. [CrossRef]
79. Webster, P.J.; Yang, S. Monsoon and Enso: Selectively Interactive Systems. *Q. J. R. Meteorol. Soc.* **1992**, *118*, 877–926. [CrossRef]
80. Barnston, A.G.; Livezey, R.E. Classification, Seasonality and Persistence of Low-Frequency Atmospheric Circulation Patterns. *Mon. Weather Rev.* **1987**, *115*, 1083–1126.<1083:CSAPOL>2.0.CO;2. [CrossRef]
81. Gao, N.; Bueh, C.; Xie, Z.; Gong, Y. A Novel Identification of the Polar/Eurasia Pattern and Its Weather Impact in May. *J. Meteorol. Res.* **2019**, *33*, 810–825. [CrossRef]
82. Lin, Z. Intercomparison of the impacts of four summer teleconnections over Eurasia on East Asian rainfall. *Adv. Atmos. Sci.* **2014**, *31*, 1366–1376. [CrossRef]
83. Gao, T.; Yu, J.y.; Paek, H. Impacts of four northern-hemisphere teleconnection patterns on atmospheric circulations over Eurasia and the Pacific. *Theor. Appl. Climatol.* **2017**, *129*, 815–831. [CrossRef]
84. Carturan, L.; Cazorzi, F.; De Blasi, F.; Dalla Fontana, G. Air temperature variability over three glaciers in the Ortles—Cevedale (Italian Alps): Effects of glacier fragmentation, comparison of calculation methods, and impacts on mass balance modeling. *Cryosphere* **2015**, *9*, 1129–1146. [CrossRef]
85. Sauter, T.; Möller, M.; Finkelnburg, R.; Grabiec, M.; Scherer, D.; Schneider, C. Snowdrift modelling for the Vestfonna ice cap, north-eastern Svalbard. *Cryosphere* **2013**, *7*, 1287–1301. [CrossRef]
86. Groot Zwaaftink, C.D.; Cagnati, A.; Crepaz, A.; Fierz, C.; Macelloni, G.; Valt, M.; Lehning, M. Event-driven deposition of snow on the Antarctic Plateau: analyzing field measurements with SNOWPACK. *Cryosphere* **2013**, *7*, 333–347. [CrossRef]
87. Olson, M.; Rupper, S. Impacts of topographic shading on direct solar radiation for valley glaciers in complex topography. *Cryosphere* **2019**, *13*, 29–40. [CrossRef]
88. Olson, M.; Rupper, S.; Shean, D.E. Terrain Induced Biases in Clear-Sky Shortwave Radiation Due to Digital Elevation Model Resolution for Glaciers in Complex Terrain. *Front. Earth Sci.* **2019**, *7*, 216. [CrossRef]
89. Beck, H.E.; Vergopolan, N.; Pan, M.; Levizzani, V.; van Dijk, A.I.J.M.; Weedon, G.P.; Brocca, L.; Pappenberger, F.; Huffman, G.J.; Wood, E.F. Global-scale evaluation of 22 precipitation datasets using gauge observations and hydrological modeling. *Hydrol. Earth Syst. Sci.* **2017**, *21*, 6201–6217. [CrossRef]

90. Kim, K.Y.; Kim, J.; Boo, K.O.; Shim, S.; Kim, Y. Intercomparison of precipitation datasets for summer precipitation characteristics over East Asia. *Clim. Dyn.* **2019**, *52*, 3005–3022. [CrossRef]
91. Immerzeel, W.W.; Wanders, N.; Lutz, A.F.; Shea, J.M.; Bierkens, M.F.P. Reconciling high altitude precipitation in the upper Indus Basin with glacier mass balances and runoff. *Hydrol. Earth Syst. Sci. Discuss.* **2015**, *12*, 4755–4784. [CrossRef]
92. Hamm, A.; Arndt, A.; Kolbe, C.; Wang, X.; Thies, B.; Boyko, O.; Reggiani, P.; Scherer, D.; Bendix, J.; Schneider, C. Intercomparison of Gridded Precipitation Datasets over a Sub-Region of the Central Himalaya and the Southwestern Tibetan Plateau. *Water* **2020**, *12*, 3271. [CrossRef]
93. Wang, X.; Tolksdorf, V.; Otto, M.; Scherer, D. WRF-based dynamical downscaling of ERA5 reanalysis data for High Mountain Asia: Towards a new version of the High Asia Refined analysis. *Int. J. Climatol.* **2020**, joc.6686. [CrossRef]
94. Hopkinson, C.; Chasmer, L.; Munro, S.; Demuth, M.N. The influence of DEM resolution on simulated solar radiation-induced glacier melt. *Hydrol. Process.* **2010**, *24*, 775–788. [CrossRef]
95. Thiel, K.; Arndt, A.; Wang, P.; Li, H.; Li, Z.; Schneider, C. Modeling of Mass Balance Variability and Its Impact on Water Discharge from the Urumqi Glacier No. 1 Catchment, Tian Shan, China. *Water* **2020**, *12*, 3297. [CrossRef]
96. Gut, A. *Probability: A Graduate Course*; OCLC: 56096548; Springer: New York, NY, USA, 2005.
97. Klok, E.; Oerlemans, J. Model study of the spatial distribution of the energy and mass balance of Morteratschgletscher, Switzerland. *J. Glaciol.* **2002**, *48*, 505–518. [CrossRef]
98. Hock, R.; Holmgren, B. A distributed surface energy-balance model for complex topography and its application to Storglaciären, Sweden. *J. Glaciol.* **2005**, *51*, 25–36. [CrossRef]
99. Machguth, H.; Paul, F.; Hoelzle, M.; Haeberli, W. Distributed glacier mass-balance modelling as an important component of modern multi-level glacier monitoring. *Ann. Glaciol.* **2006**, *43*, 335–343. [CrossRef]
100. Reijmer, C.H.; Hock, R. Internal accumulation on Storglaciären, Sweden, in a multi-layer snow model coupled to a distributed energy-and mass-balance model. *J. Glaciol.* **2008**, *54*, 61–72. [CrossRef]
101. Sicart, J.E.; Hock, R.; Ribstein, P.; Litt, M.; Ramirez, E. Analysis of seasonal variations in mass balance and meltwater discharge of the tropical Zongo Glacier by application of a distributed energy balance model. *J. Geophys. Res.* **2011**, *116*, D13105. [CrossRef]
102. Van Pelt, W.J.J.; Oerlemans, J.; Reijmer, C.H.; Pohjola, V.A.; Pettersson, R.; van Angelen, J.H. Simulating melt, runoff and refreezing on Nordenskiöldbreen, Svalbard, using a coupled snow and energy balance model. *Cryosphere* **2012**, *6*, 641–659. [CrossRef]
103. Yao, T.D.; Pu, J.C.; Tian, L.D.; Yang, W.; Duan, K.Q.; Ye, Q.H.; Thompson, L.G. Recent Rapid Retreat of the Naimona'nyi Glacier in Southwestern Tibetan Plateau. *J. Glaciol. Geocryol.* **2007**, *29*, 503–508.
104. Zhu, D.; Tian, L.; Wang, J.; Wang, Y.; Cui, J. Rapid glacier retreat in the Naimona'Nyi region, western Himalayas, between 2003 and 2013. *J. Appl. Remote Sens.* **2014**, *8*, 083508. [CrossRef]
105. Priya, P.; Krishnan, R.; Mujumdar, M.; Houze, R.A. Changing monsoon and midlatitude circulation interactions over the Western Himalayas and possible links to occurrences of extreme precipitation. *Clim. Dyn.* **2017**, *49*, 2351–2364. [CrossRef]
106. Bothe, O.; Fraedrich, K.; Zhu, X. Tibetan Plateau summer precipitation: Covariability with circulation indices. *Theor. Appl. Climatol.* **2012**, *108*, 293–300. [CrossRef]
107. Liu, W.; Wang, L.; Chen, D.; Tu, K.; Ruan, C.; Hu, Z. Large-scale circulation classification and its links to observed precipitation in the eastern and central Tibetan Plateau. *Clim. Dyn.* **2016**, *46*, 3481–3497. [CrossRef]
108. Palazzi, E.; von Hardenberg, J.; Provenzale, A. Precipitation in the Hindu-Kush Karakoram Himalaya: Observations and future scenarios: PRECIPITATION IN HINDU-KUSH KARAKORAM HIMALAYA. *J. Geophys. Res. Atmos.* **2013**, *118*, 85–100. [CrossRef]
109. Kajikawa, Y.; Wang, B.; Yang, J. A multi-time scale Australian monsoon index: A MULTI-TIME SCALE AUSTRALIAN MONSOON INDEX. *Int. J. Climatol.* **2010**, *30*, 1114–1120. [CrossRef]
110. Enfield, D.B.; Mestas-Nuñez, A.M.; Trimble, P.J. The Atlantic Multidecadal Oscillation and its relation to rainfall and river flows in the continental U.S. *Geophys. Res. Lett.* **2001**, *28*, 2077–2080. [CrossRef]
111. Thompson, D.W.J.; Wallace, J.M. The Arctic oscillation signature in the wintertime geopotential height and temperature fields. *Geophys. Res. Lett.* **1998**, *25*, 1297–1300. [CrossRef]
112. Bureau of Meteorology, Commonwealth of Australia. *About ENSO and IOD Indices*; Online Resources (2021): Bureau of Meteorology, Commonwealth of Australia. Available online: http://www.bom.gov.au/climate/enso/indices/about.shtml (accessed on 22 March 2021).
113. Wang, B.; Fan, Z. Choice of South Asian Summer Monsoon Indices*. *Bull. Am. Meteorol. Soc.* **1999**, *80*, 629–638. [CrossRef]
114. Wang, B.; Wu, R.; Lau, K.M. Interannual Variability of the Asian Summer Monsoon: Contrasts between the Indian and the Western North Pacific–East Asian Monsoons*. *J. Clim.* **2001**, *14*, 4073–4090. [CrossRef]
115. Zhang, T.; Hoell, A.; Perlwitz, J.; Eischeid, J.; Murray, D.; Hoerling, M.; Hamill, T.M. Towards Probabilistic Multivariate ENSO Monitoring. *Geophys. Res. Lett.* **2019**, *46*, 10532–10540. [CrossRef]
116. Hurrell, J.W. Decadal Trends in the North Atlantic Oscillation: Regional Temperatures and Precipitation. *Science* **1995**, *269*, 676–679. [CrossRef]
117. Trenberth, K.E.; Stepaniak, D.P. Indices of El Niño Evolution. *J. Clim.* **2001**, *14*, 1697–1701. [CrossRef]
118. Mantua, N.J.; Hare, S.R. The Pacific Decadal Oscillation. *J. Oceanogr.* **2002**, *58*, 35–44. [CrossRef]

119. Wallace, J.M.; Gutzler, D.S. Teleconnections in the Geopotential Height Field during the Northern Hemisphere Winter. *Mon. Weather Rev.* **1981**, *109*, 784–812. [CrossRef]
120. National Oceanic and Atmospheric Administration. *Southern Oscillation Index (SOI)*; Online Resources (2021): National Oceanic and Atmospheric Administration. Available online: https://www.ncdc.noaa.gov/teleconnections/enso/indicators/soi/ (accessed on 22 March 2021).